Supporting Information

Sensitization-initiated electron transfer via upconversion: Mechanism and photocatalytic applications

Felix Glaser, Christoph Kerzig and Oliver S. Wenger *

Table of Contents

1. General experimental details

All deuterated solvents were purchased from Cambridge Isotope Laboratories Inc. Reagents were purchased from Fluorochem, AmBeed, Alfar Aesar, Acros Organics or Sigma-Aldrich/Merck in "reagent grade" purity or better and were used as received. DMF was purchased "extra dry" in 99.8% purity from Acros Organics and was used for photocatalytic reactions as well as spectroscopic measurements.

All NMR spectra were recorded on a Bruker Avance III instrument operating at 400 MHz proton frequency. All samples were recorded at 295 K in 5 mm diameter tubes. Chemical shifts (^{1}H-NMR) were referenced internally to residual solvent peaks using δ values as reported by GOTTLIEB *et al* or the internal standard.[1] Starting material consumption and product formation were determined from ^{19}F-NMR measurements (^{19}F: 376 MHz, 16 scans) in NMR tubes against 4-fluorotoluene (-119.15 ppm) as internal standard.

Sample preparation for photoreduction reactions and spectrophotometric measurements were performed in screw cap quartz cuvettes. All solutions were purged with argon to remove oxygen and sealed under argon with septum caps. For photocatalytic reactions, a balloon with argon was installed during the time of the reaction.

Absorption spectra were recorded on a Cary 5000 UV-Vis-NIR spectrometer from Varian. Photoluminescence spectra were recorded on a Fluorolog-322 instrument from Horiba Jobin-Yvon. For laser flash photolysis, an LP920-KS apparatus from Edinburgh Instruments was used. A frequency-tripled Nd:YAG laser (Quantel Brilliant, ca. 10 ns pulse width) equipped with an OPO from Opotek and a beam expander (GBE02-A from Thorlabs) in the beam path was used for excitation with visible light. The direct output of another frequency-tripled Nd:YAG laser (Quantel Q-smart 450 mJ, ca. 10 ns pulse width) with a beam expander (BE02-355 from Thorlabs) in the beam path was used for excitation at 355 nm. The excitation energies were varied by the Q-switch delays and measured with a pyroelectric detector. Typically, pulse energies between 10 mJ and 15 mJ were used for the measurements with visible light, and pulse energies of 5 mJ to 50 mJ were used for the measurements with 355 nm excitation. Detection of transient absorption and time-resolved emission spectra was performed with an iCCD camera (Andor). Kinetics at single wavelengths were recorded using a photomultiplier tube. Photoluminescence quantum yields were measured on a Hamamatsu absolute PL quantum yield spectrometer C11347 Quantaurus-QY in de-aerated solutions.

Cyclic voltammetry was performed using a Versastat3-200 potentiostat from Princeton Applied Research. A saturated calomel electrode (SCE) served as reference electrode, a glassy carbon disk electrode was employed as working electrode, and a silver wire was used as counter electrode. Measurements were performed with potential sweep rates of 100 mV/s in dry de-aerated solvent with 0.1 M TBAPF$_6$ (tetra-*n*-butylammonium hexafluorophosphate) as supporting electrolyte. Sample concentrations were adjusted to values between 1 mM and 5 mM.

Spectro-electrochemical measurements were performed in a quartz cuvette using the potentiostat and the UV-Vis-NIR spectrometer mentioned above. A platinum grid served as working electrode, a platinum wire was used as counter electrode and an SCE was employed as reference electrode.

For the measurements of the triplet-triplet annihilation upconversion power dependencies and the photostabilities, the Fluorolog-3-22 was equipped with a 447 nm continuous wave (cw) laser (Roithner Lasertechnik) as light source with precisely adjustable radiative power (optical output up to 1070 mW) and high output stability (< 1 %). The unmodified laser beam (5.0 × 2.5 mm) was used for the experiments presented herein. The maximum power density is thus estimated to ca. 8.5 W cm^{-2}.

As light source for cw-laser experiments in photocatalysis, the same 447 nm cw-laser was used as light source and a beam expander (GBE05-A from Thorlabs) was installed backwards in the beam path to obtain a compressed laser beam with up to 42.5 W cm^{-2} power density. An output spectrum of this laser has been reported previously.[2] For measurements with a 440 nm LED, a Kessil PR160 LED (40 W) was used, and two 400 nm long-pass filters (coloured glass 400 nm cut-off filter, Reichmann Feinoptik GmbH) were installed between the lamp and the sample. An output spectrum of the LED has been reported previously.[3]

2. Spectroscopic measurements

2.1. Spectroscopic properties of *fac*-[Ir(ppy)$_3$] and ^{tBu}Py

2.1.1. Photophysical characterization in DMF

All following measurements were performed in de-aerated DMF at room temperature.

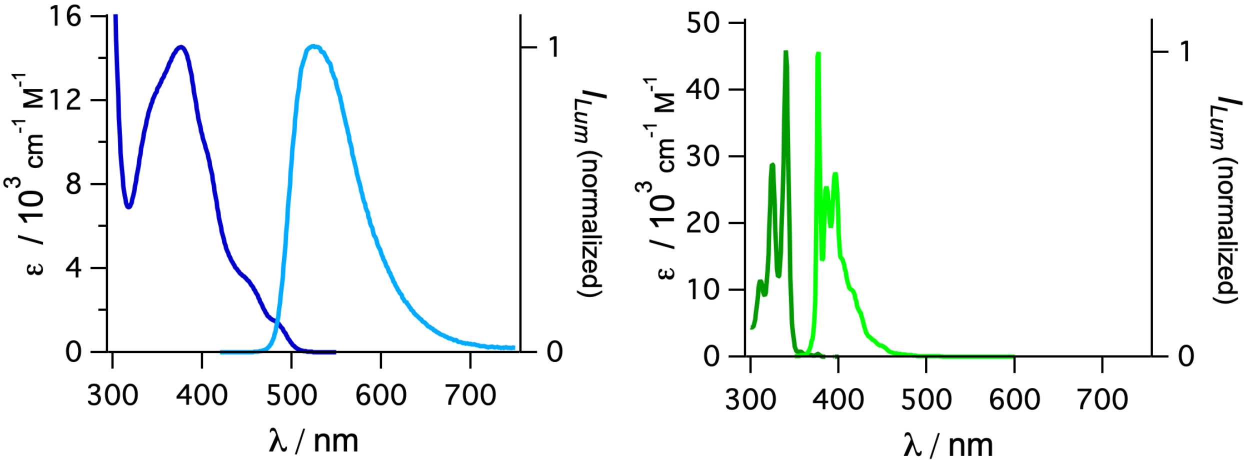

Figure S1. UV-vis absorption (dark blue and dark green traces) and emission spectra (light blue and light green traces) of *fac*-[Ir(ppy)$_3$] (left) and ^{tBu}Py (right) in de-aerated DMF. Excitation occurred at 400 nm in the case of *fac*-[Ir(ppy)$_3$] and at 340 nm in the case of ^{tBu}Py.

Table S1. Overview of photophysical properties of *fac*-[Ir(ppy)$_3$] and ^{tBu}Py in de-aerated DMF at 20 °C.

compound	λ_{abs} (ε) / nm (M^{-1} s^{-1})	λ_{em} (ϕ) / nm (%)	τ_0 / ns
fac-[Ir(ppy)$_3$]	376 (14 500)	525 (88)	1590
^{tBu}Py	340 (45 900)	377 (59)	230

Absorption spectra, emission spectra, luminescence quantum yields and excited-state lifetimes (**Figure S1** and **Table S1**) for *fac*-[Ir(ppy)$_3$] and ^{tBu}Py were similar as in prior studies in DMF or other polar solvents.[4–6]

2.1.2. Photostability measurements in DMF

We investigated the photostabilities of *fac*-[Ir(ppy)$_3$] and the upconversion system by measuring the luminescence intensity of *fac*-[Ir(ppy)$_3$] and ^{1*tBu}Py as a function of irradiation time (**Figure S2**). The luminescence intensities were recorded on our emission spectrometer under cw-laser irradiation (447 nm, 1070 mW) in a similar setup as reported previously.[7] Neutral density filters (Newport) were installed in front of the detector to adjust the respective emission intensity to the linear regime of our detector.

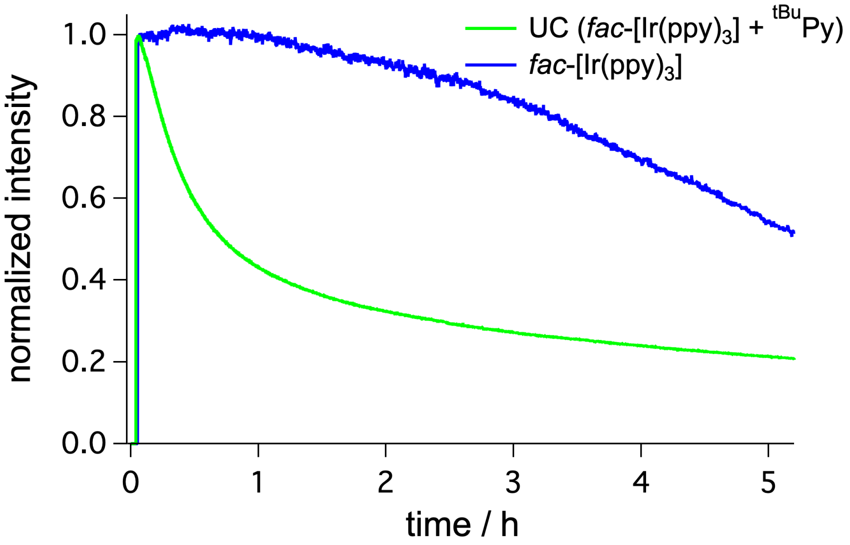

Figure S2. Emission intensity changes over time of *fac*-[Ir(ppy)$_3$] (30 µM, blue trace) at 525 nm and the upconverted emission of *fac*-[Ir(ppy)$_3$] (30 µM) with ^{tBu}Py (5 mM, green trace) at 395 nm in de-aerated DMF under cw-laser irradiation (447 nm, 1070 mW) at 20 °C.

2.2. Triplet-triplet energy transfer from *fac*-[Ir(ppy)$_3$] to ^{tBu}Py

Further information to step 1 in Figure 2 of the main manuscript is presented here.

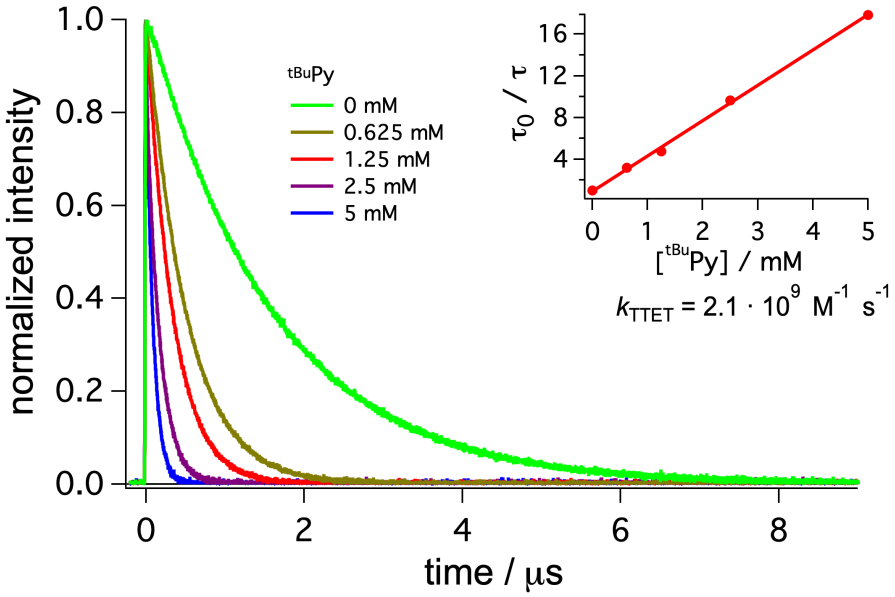

Figure S3. Fluorescence quenching of *fac*-[Ir(ppy)$_3$] by ^{tBu}Py. *fac*-[Ir(ppy)$_3$] (10 µM) in de-aerated DMF was excited at 450 nm. The emission decay was monitored at 515 nm in the absence (green) and in the presence of different concentrations of ^{tBu}Py as indicated in the inset. The inset in the upper right corner contains the resulting Stern-Volmer plot and the calculated quenching rate constant.

Stern-Volmer analysis of the energy transfer of *fac*-[Ir(ppy)$_3$] with ^{tBu}Py results in a quenching rate constant k_{TTET} of $2.1 \cdot 10^9$ M^{-1} s^{-1} (**Figure S3**). Triplet-triplet energy transfer (TTET) from *fac*-[Ir(ppy)$_3$] to a substituted pyrene has been previously explored in DCM and resulted in a similar rate constant ($9.78 \cdot 10^8$ M^{-1} s^{-1}).[8] Transient absorption spectra recorded with a time delay of 10 µs reveal the formation of the lowest triplet excited state of ^{tBu}Py (**Figure S4**), with its characteristic absorption band at 416 nm.[9] With increasing concentration of ^{tBu}Py, the rate of formation of triplet-excited ^{tBu}Py increases (**Figure S4**, right inset). This is in line with the proposed energy transfer mechanism.

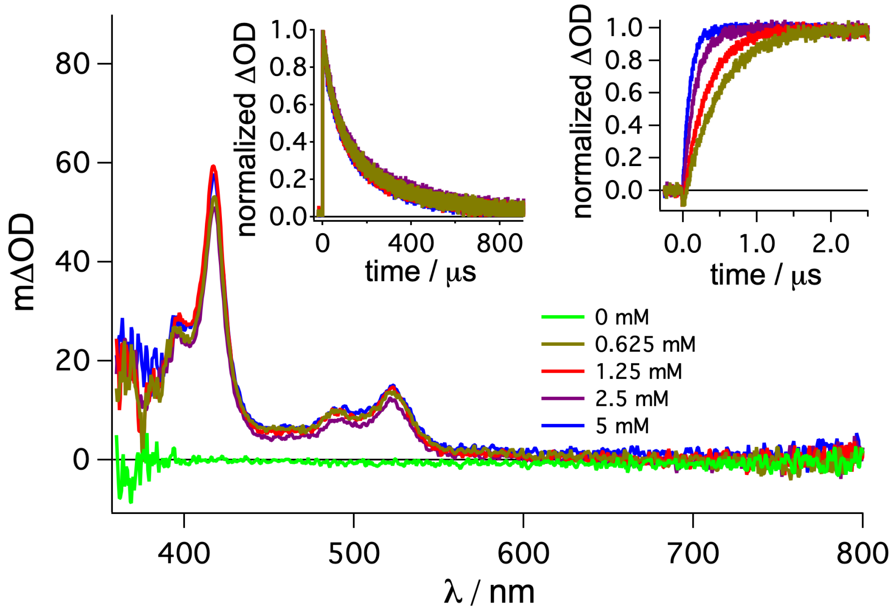

Figure S4. Triplet state formation and decay of ^{tBu}Py. *fac*-[Ir(ppy)$_3$] (10 µM) in de-aerated DMF was excited at 450 nm and the transient absoprtion spectra were recorded with a time delay of 10 µs, time-integrated over 200 ns. Different concentrations of ^{tBu}Py were used (color code for all parts in the main part of the figure). The left inset exhibits the decays of the lowest triplet excited state of ^{tBu}Py (as monitored at 416 nm) after triplet-triplet energy transfer from *fac*-[Ir(ppy)$_3$]. The right inset displays the signal growth monitored at the same wavelenth within the first 2.5 µs after the laser pulse, corresponding to the formation of ^{3*tBu}Py.

2.3. Reductive quenching of *fac*-[Ir(ppy)$_3$] by DMA

This subsection contains additional data concerning step 1b in Figure 2 of the main manuscript.

Reductive quenching of excited *fac*-[Ir(ppy)$_3$] by DMA is very inefficient based on a Stern-Volmer quenching experiment, yielding a quenching rate constant of only $1.1 \cdot 10^4$ M^{-1} s^{-1} (**Figure S5**). The highest concentration of DMA during these luminescence-quenching measurements (125 mM) is close to the concentration under photocatalytic conditions (150 mM, see Table 2 of the main manuscript).

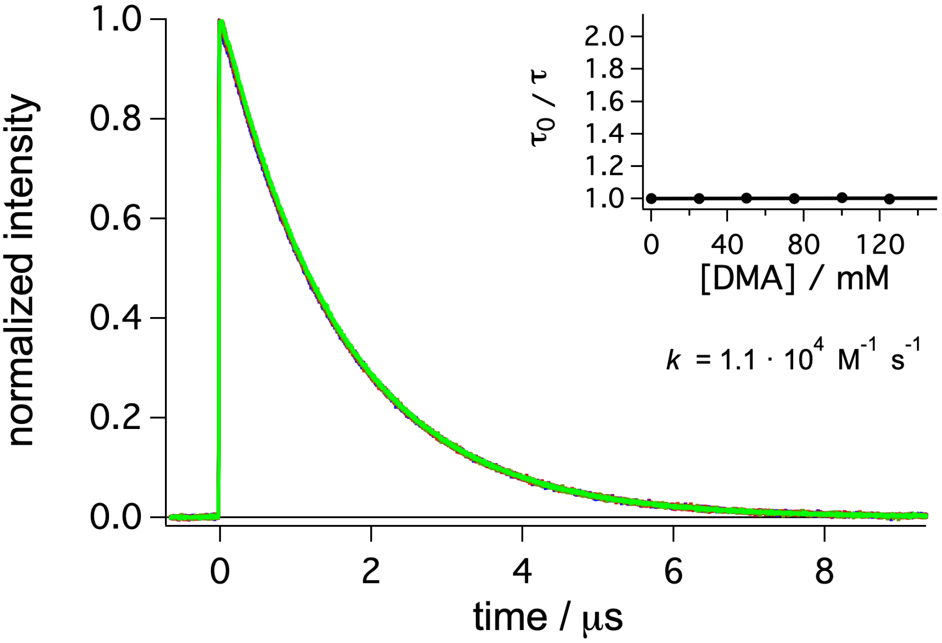

Figure S5. Fluorescence quenching of *fac*-[Ir(ppy)$_3$] by DMA. *fac*-[Ir(ppy)$_3$] (10 µM) in de-aerated DMF was excited at 450 nm and the emission decay was monitored at 515 nm in the absence (green) and in the presence of different concentrations of DMA (25, 50, 75, 100, 125 mM). The inset displays the resulting Stern-Volmer plot and the calculated quenching rate constant.

2.4. Triplet state quenching of ^{tBu}Py by DMA

Further information for the results corresponding to step 2b in Figure 2 of the main manuscript is given here.

No reductive quenching of ^{3*tBu}Py by DMA is observable (**Figure S6**). ^{3*tBu}Py can decay via two different pathways: (i) direct decay to the electronic ground state (a first-order process associated with a specific natural lifetime), and (ii) via triplet-triplet annihilation, corresponding to a second-order process. Consequently, a straightforward Stern-Volmer analysis is not possible. However, up to a DMA concentration of 125 mM, the kinetic decays of ^{3*tBu}Py sensitized by *fac*-[Ir(ppy)$_3$] are unchanged (**Figure S6**), and from this we conclude that electron transfer from DMA to ^{3*tBu}Py occurs with a rate constant that is at most on the order of 10^3 M^{-1} s^{-1}. The highest DMA concentration in these measurements (125 mM) is close to the concentration used for the photocatalytic experiments (150 mM, see Table 2 of the main manuscript), indicating that reductive quenching of ^{3*Bu}Py by DMA is no relevant process in our catalytic systems.

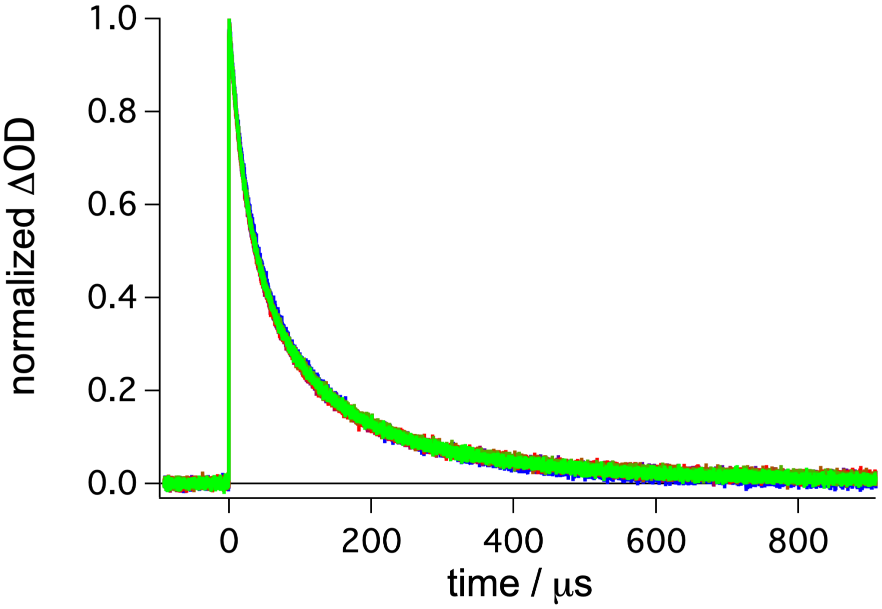

Figure S6. Triplet state decay of ^{tBu}Py. *fac*-[Ir(ppy)$_3$] (10 μM) in de-aerated DMF was excited at 450 nm in the presence of ^{tBu}Py (5 mM) and the triplet state decay of ^{tBu}Py was monitored at 416 nm in the absence (green) and in the presence of different concentrations of DMA (25, 50, 75, 100, 125 mM).

2.5. Triplet-triplet annihilation upconversion

Further information concerning step 2 in Figure 2 of the main manuscript is given here. This section is divided into three subsections that cover the determination of the rate constant for triplet-triplet annihilation (2.5.1), the quadratic power dependence of the upconversion step (2.5.2) and the estimation of the upconversion quantum yield (2.5.3).

2.5.1. The rate constant for triplet-triplet annihilation

As discussed above, ^{3*tBu}Py decays via two concurrent pathways, including ordinary first-order decay (natural lifetime of triplet, τ_0 (= 1/k_T)) and a second-order process (triplet-triplet annihilation, k_{TTA}). Bachilo and Weisman derived an analytical solution (equation S1) taking both concurrent processes into account.[10] They define a dimensionless parameter β (equation S2) as the fraction of the decay that takes place through triplet-triplet annihilation.

$$[^3A]_t = \frac{[^3A]_0 \cdot (1-\beta)}{\exp(k_T \cdot t) - \beta} \qquad \textbf{(S1)}$$

$$\beta = \frac{k_{TTA} \cdot [^3A]_0}{k_{TTA} \cdot [^3A]_0 + k_T} \qquad \textbf{(S2)}$$

The extinction coefficient for ${}^{3*\mathrm{tBu}}$Py at its characteristic absorption maximum does not seem to be known. Therefore, we estimated the initial triplet concentration ($[{}^{3}A]_0$) based on the extinction coefficient of unsubstituted pyrene (37700 M^{-1} s^{-1} at 415 nm)[11] and the initial transient absorbance value (maximum of each kinetic trace in **Figure S7**) at that wavelength. Ordinary (unsubstituted) pyrene and ${}^{\mathrm{tBu}}$Py have nearly identical triplet absorption spectra, and it seems reasonable to use the extinction coefficient of unsubstituted pyrene at 415 nm as a proxy for the unknown extinction coefficient of ${}^{\mathrm{tBu}}$Py. Calculation of the rate constant for triplet-triplet annihilation can be achieved by fitting of the time-resolved data of kinetic traces at 415 nm with different initial triplet state concentrations according to equation S1.[2,7,12] Variation of the laser pulse energies was used to change the initial triplet concentration, and the values resulting from the individual fits of each decay curve were averaged to obtain a triplet-triplet annihilation rate constant k_{TTA} of $(1.1 \pm 0.2) \cdot 10^{10}$ M^{-1} s^{-1}. The natural lifetime of ${}^{3*\mathrm{tBu}}$Py is obtained from the same fit curves (using $\tau_0 = 1/k_{\mathrm{T}}$). The measured data as well as the fit curves (dashed green traces) are included in **Figure S7**. Our calculated triplet-triplet annihilation rate constant is on the same order of magnitude as that previously reported by Moore and coworkers for unsubstituted pyrene in DMSO ($k_{\mathrm{TAA}} = 1.34 \cdot 10^{10}$ M^{-1} s^{-1}).[13]

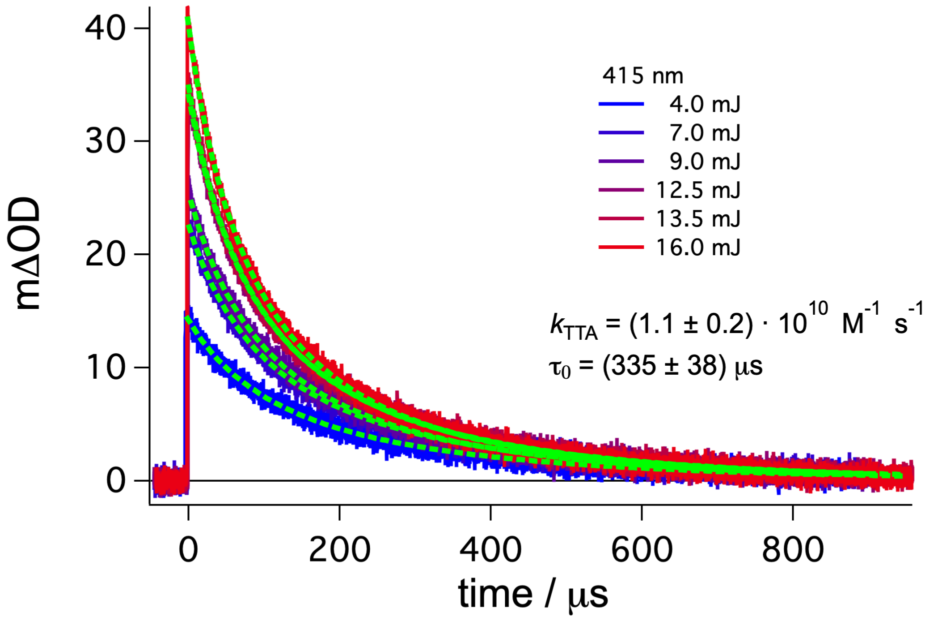

Figure S7. Power-dependent triplet state decay of ${}^{\mathrm{tBu}}$Py. *fac*-[Ir(ppy)$_3$] (10 µM) in de-aerated DMF was excited at 450 nm in the presence of ${}^{\mathrm{tBu}}$Py (5 mM). Decay of transient signals of ${}^{3*\mathrm{tBu}}$Py recorded with different excitation pulse energies (see inset) were monitored at 415 nm. Fitting curves are displayed as dashed green traces (see text for details).

2.5.2. Quadratic power dependence of upconversion step

In theory a quadratic dependence of the upconverted emission based on the excitation intensity can be excepted for small excitation power densities.[14,15] Using a stock solution of *fac*-[Ir(ppy)$_3$] (10 µM) in DMF two samples were prepared, one containing ^{tBu}Py (1 mM) while the other one did not. Both solutions were excited at 450 nm with the internal light source of our Fluorolog instrument, and the light intensity was varied by introducing neutral density filters (Thorlabs) in the excitation beam path. The prompt *fac*-[Ir(ppy)$_3$] emission was recorded between 460 nm and 750 nm while the upconverted delayed fluorescence emitted by ^{tBu}Py was detected between 360 nm to 430 nm (**Figure S8**). Relative integrated emission intensities were determined by integration of the emission spectra displayed on a wavenumber scale. The resulting relative integrated emission intensities were then plotted as a function of the relative excitation power densities (insets of **Figure S8**). Fitting of these data with a power function ($y(x) = a \cdot x^b + y_0$) results in a nearly quadratic dependence of 1.96 for the upconverted emission intensity (inset from left part of **Figure S8**) while a linear dependence of 1.00 is found for the *fac*-[Ir(ppy)$_3$] emission (inset from right part of **Figure S8**).

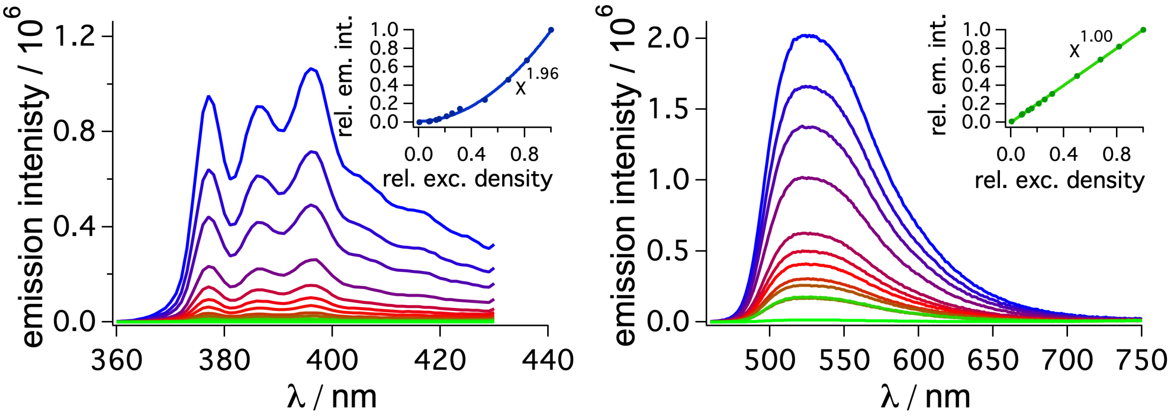

Figure S8. Power dependence of emission intensities. Emission spectra of *fac*-[Ir(ppy)$_3$] (10 μM) in de-aerated DMF upon variation of the irradiation power (right) and delayed emission spectra of upconverted emission for an identical solution with ^{tBu}Py (1 mM) added additionally (left) are shown. Both solutions were excited at 450 nm with the internal light source of the instrument (450 W xenon lamp, 12 nm excitation slit width in the absence of ^{tBu}Py (right data set) and 13 nm excitation slit width in the presence of ^{tBu}Py (left data set)), and excitation power densities were changed with reflective neutral density filters (Thorlabs). The insets display the respective integrated relative emission intensities in dependence of the excitation power densities (green and blue circles) and the corresponding best power function fit result (fit function $y(x) = a \cdot x^b + y$; fit curves in green and blue). The two insets of this figure present the same data as Figure 4D of the main manuscript.

We used the internal light source of our instrument for excitation of our samples, as this is much weaker than our 447 nm cw-laser. With the latter a linear power-dependence was found for both solutions (data not shown), suggesting that the strong annihilation limit for upconversion processes is reached under cw-laser excitation conditions.[15] Measurements with a 440 nm LED (Kessil) at full power also resulted in a linear power dependence for upconverted light (data not shown).

2.5.3. Upconversion quantum yield estimation

Based on the output power calibration sheet provided by the laser manufacturer (Roithner Lasertechnik), the precisely adjustable power of the 447 nm cw-laser was used for the relative quantum yield determination of the upconverted emission of our system in comparison to the emission quantum yield of *fac*-[Ir(ppy)$_3$] in de-aerated DMF (88 %, determined as absolute quantum yield, see section 2.1). A description of a similar setup has been reported recently.[7] Neutral density filters were employed to attenuate emission intensities where necessary, and to attenuate the laser excitation power below 80 mW.

An upconversion quantum yield $\phi_{\mathrm{sTAA\text{-}UC}}$ of ~4.8 % for the delayed $^{1*\mathrm{tBu}}$Py emission is achievable with this system (**Figure S9**), using a theoretical limit of 50 % as suggested recently.[16] A detailed discussion is provided in the main manuscript. Taking into account that the fluorescence quantum yield of $^{1*\mathrm{tBu}}$Py in de-aerated DMF at 20 °C is 59 % (see section 2.1), about ~8 % of $^{1*\mathrm{tBu}}$Py are obtained.

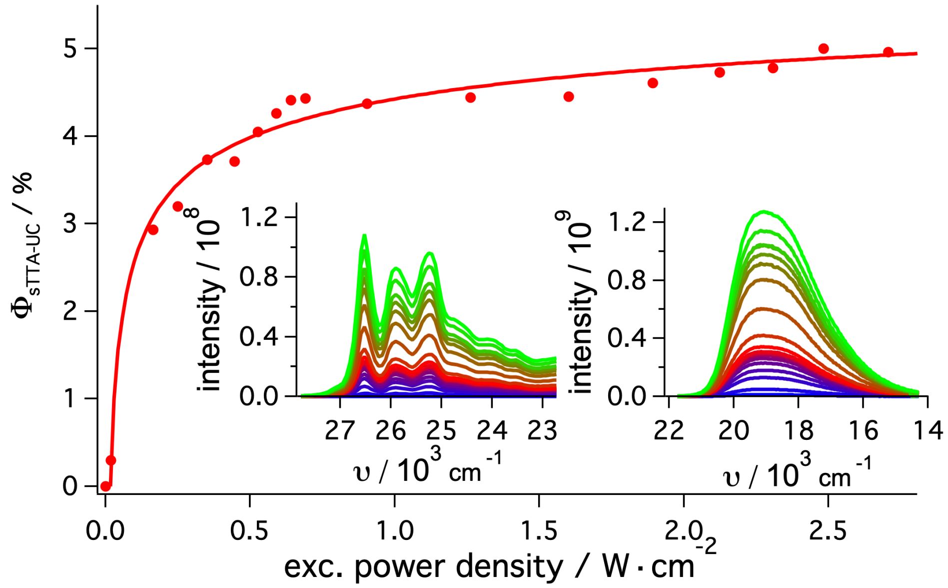

Figure S9. Upconversion quantum yield ($\phi_{\mathrm{sTTA\text{-}IC}}$) of *fac*-[Ir(ppy)$_3$] (30 μM) and $^{\mathrm{tBu}}$Py (5 mM) in DMF upon variation of the excitation power density. The insets show the corresponding emission spectra in wavenumbers for upconverted $^{\mathrm{tBu}}$Py emission (left) as well as emission of *fac*-[Ir(ppy)$_3$] in the absence of annihilator (reference system, right). These are the same data sets as in Figure 4A-C of the main manuscript.

2.6. Reductive quenching of $^{1*\mathrm{tBu}}$Py by DMA

Further information for the results corresponding to step 3 in Figure 2 of the main manuscript is given here.

$^{1*\mathrm{tBu}}$Py is quenched by DMA with a rate constant of $4.8 \cdot 10^9$ M^{-1} s^{-1} (**Figure S10**).

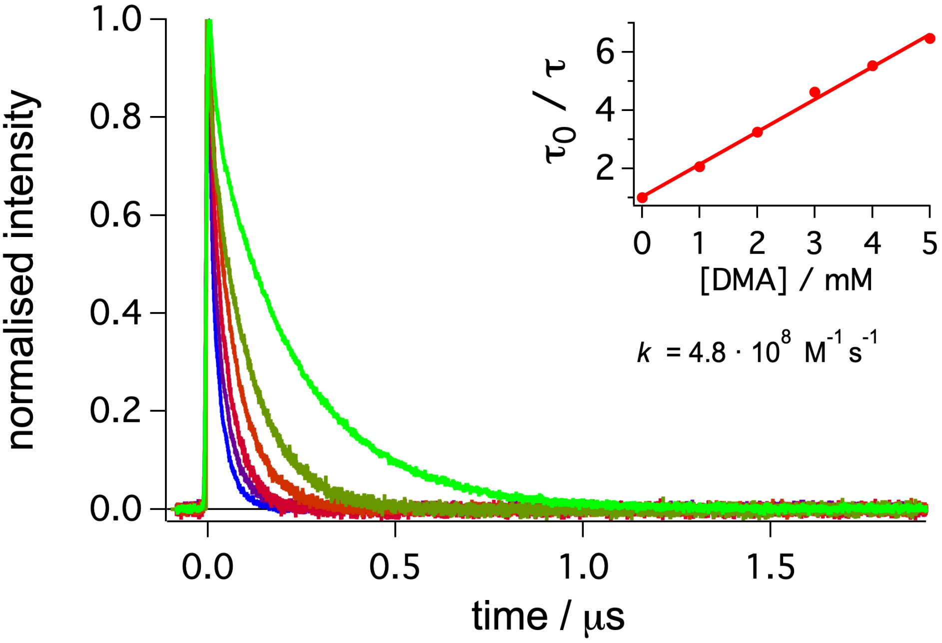

Figure S10. Fluorescence quenching of ^{tBu}Py by DMA. ^{tBu}Py (50 µM) in de-aerated DMF was excited at 355 nm and the emission decay was monitored at 395 nm in the absence (green) and in the presence of different concentrations of DMA (1, 2, 3, 4, 5 mM). The Stern-Volmer plot obtained from this data set and the resulting quenching constant are given in the inset.

2.7. Oxidative quenching of ^{1*tBu}Py by different substrates

Further information for the results corresponding to step 3b in Figure 2 of the main manuscript is given here.

Table S2. Rate constants (k_Q) for reductive quenching of ^{1*tBu}Py by DMA and for oxidative quenching by the different explored substrates in de-aerated DMF.

entry	substrate	k_Q / M^{-1} s^{-1}	data set presented in
1	DMA	$4.8 \cdot 10^9$	**Figure S10**
2	2-chloro-4-fluorobenzonitrile (**1**)	$6.4 \cdot 10^7$	**Figure S11**
3	2-bromo-4-fluorobenzonitrile (**2**)	$3.9 \cdot 10^8$	**Figure S12**
4	4-bromo-2-fluorobenzonitrile (**3**)	$2.1 \cdot 10^9$	**Figure S13**
5	4-fluoroacetophenone (**4**)	$9.4 \cdot 10^7$	**Figure S14**
6	*N*-(2-fluorophenyl)-4-methylbenzenesulfonamide (**5**)	$1.1 \cdot 10^7$	**Figure S15**

The following Stern-Volmer plots (insets of respective figures) are all drawn on the same x- and y-scales to simplify a visual comparison between the different data sets.

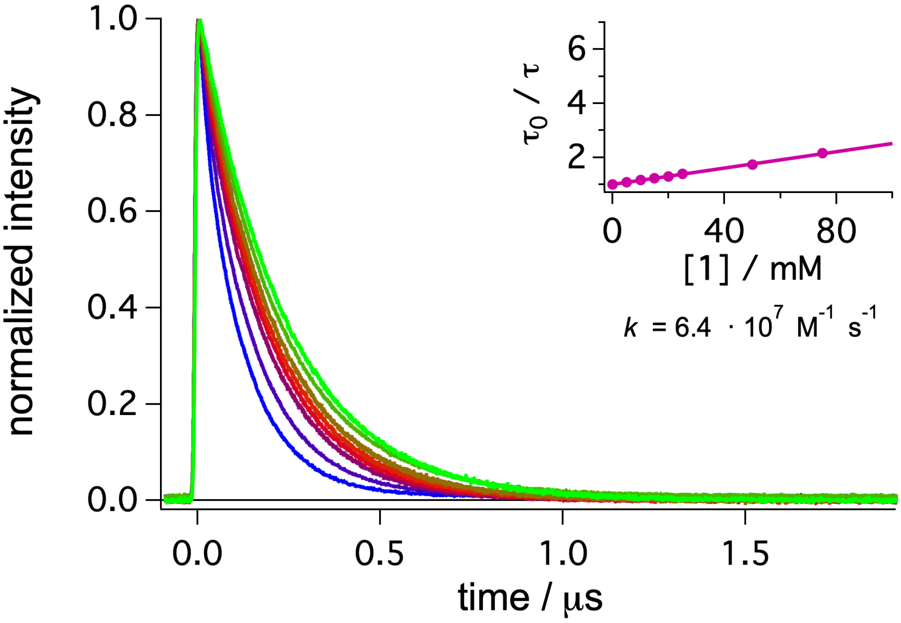

Figure S11. Fluorescence quenching of ^{tBu}Py by substrate **1**. ^{tBu}Py (50 µM) in de-aerated DMF was excited at 355 nm and the emission decay was monitored at 395 nm in the absence (green) and in the presence of different concentrations of **1** (5, 10, 15, 20, 25, 50, 75 mM). The Stern-Volmer plot obtained from this data set and the resulting quenching rate constant are given in the inset.

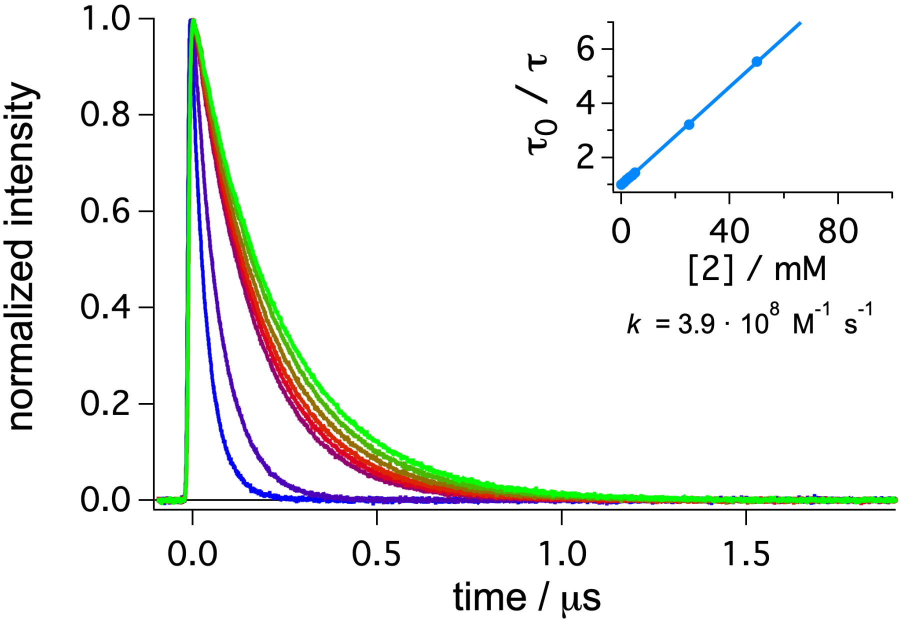

Figure S12. Fluorescence quenching of ^{tBu}Py by substrate **2**. ^{tBu}Py (50 µM) in de-aerated DMF was excited at 355 nm and the emission decay was monitored at 395 nm in the absence (green) and in the presence of different concentrations of **2** (1, 2, 3, 4, 5, 25, 50 mM). The Stern-Volmer plot obtained from this data set and the resulting quenching rate constant are given in the inset.

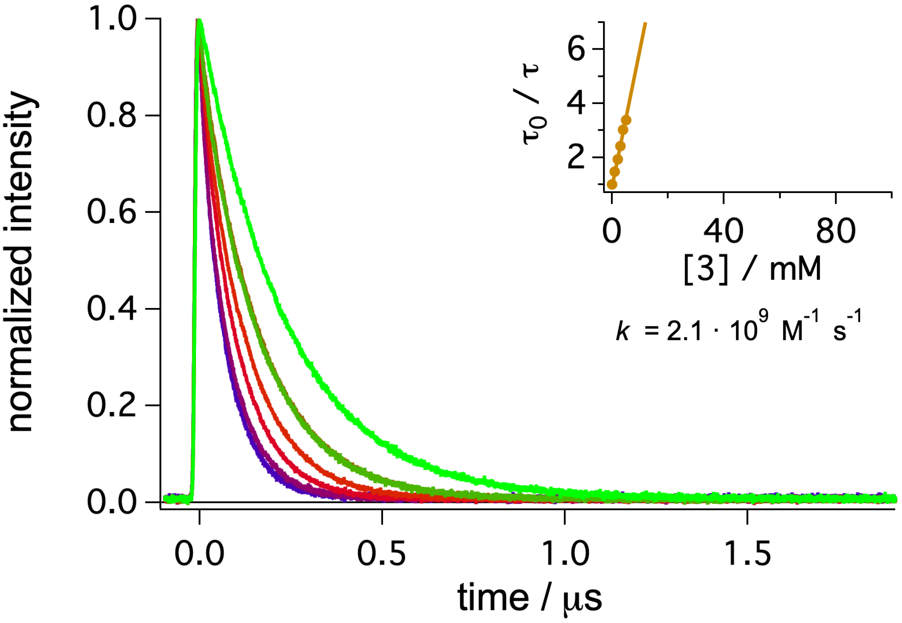

Figure S13. Fluorescence quenching of ^{tBu}Py by substrate **3**. ^{tBu}Py (50 µM) in de-aerated DMF was excited at 355 nm and the emission decay was monitored at 395 nm in the absence (green) and in the presence of different concentrations of **3** (1, 2, 3, 4, 5, mM). The Stern-Volmer plot obtained from this data set and the resulting quenching rate constant are given in the inset.

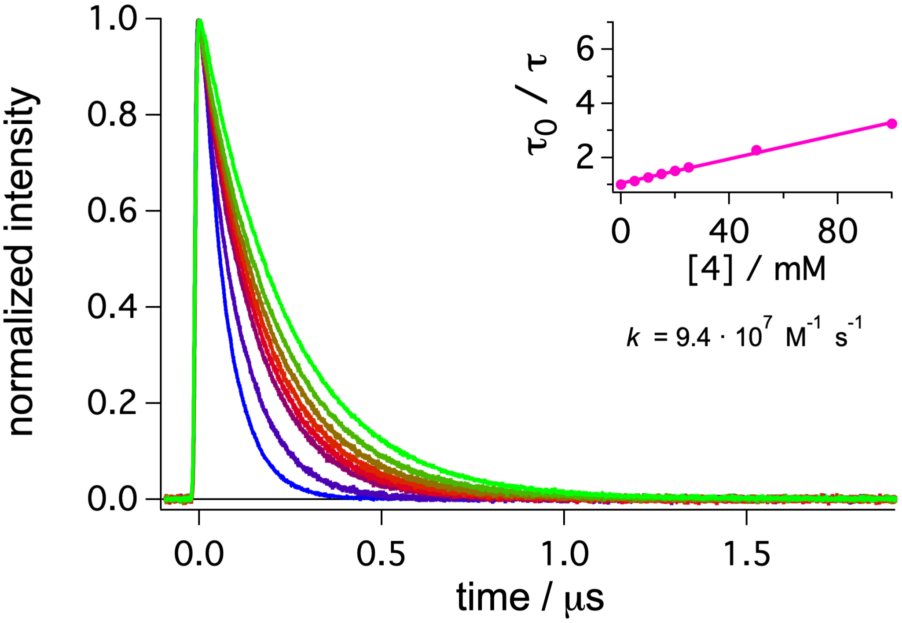

Figure S14. Fluorescence quenching of ^{tBu}Py by substrate **4**. ^{tBu}Py (50 µM) in de-aerated DMF was excited at 355 nm and the emission decay was monitored at 395 nm in the absence (green) and in the presence of different concentrations of **4** (5, 10, 15, 20, 25, 50, 100 mM). The Stern-Volmer plot obtained from this data set and the resulting quenching rate constant are given in the inset.

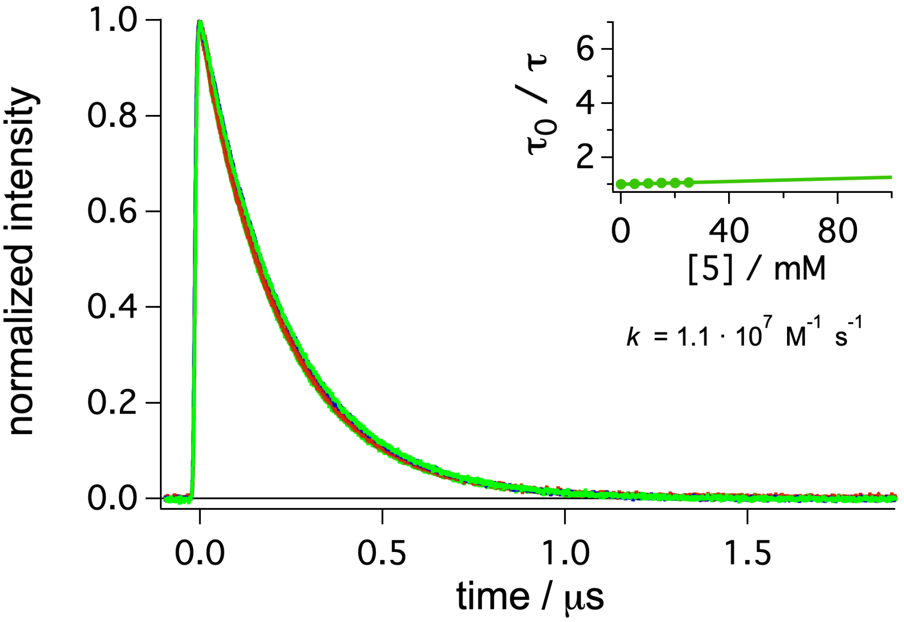

Figure S15. Fluorescence quenching of ^{tBu}Py by substrate **5**. ^{tBu}Py (50 µM) in de-aerated DMF was excited at 355 nm and the emission decay was monitored at 395 nm in the absence (green) and in the presence of different concentrations of **5** (5, 10, 15, 20, 25 mM). The Stern-Volmer plot obtained from this data set and the resulting quenching rate constant are given in the inset.

2.8. Oxidative excited-state quenching of *fac*-[Ir(ppy)$_3$] by different substrates

Further information for the results corresponding to step 1c in Figure 2 of the main manuscript is given here.

Table S3. Rate constants (k_Q) for excited-state quenching of *fac*-[Ir(ppy)$_3$] in de-aerated DMF by DMA and by the different substrates.

entry	substrate	k_Q / M^{-1} s^{-1}	data set presented in
1 [a]	DMA	$1.1 \cdot 10^4$	**Figure S5**
2 [b]	2-chloro-4-fluorobenzonitrile (**1**)	$9.8 \cdot 10^5$	**Figure S16**
3 [b]	2-bromo-4-fluorobenzonitrile (**2**)	$6.4 \cdot 10^6$	**Figure S17**
4 [b]	4-bromo-2-fluorobenzonitrile (**3**)	$4.4 \cdot 10^6$	**Figure S18**
5 [b]	4-fluoroacetophenone (**4**)	$2.1 \cdot 10^4$	**Figure S19**
6 [b]	*N*-(2-fluorophenyl)-4-methylbenzenesulfonamide (**5**)	$4.1 \cdot 10^5$	**Figure S20**

(a) Reductive quenching. (b) Oxidative quenching.

The following Stern-Volmer plots (insets of respective figures) are all drawn on the same x- and y-scales to simplify a visual comparison between the different data sets.

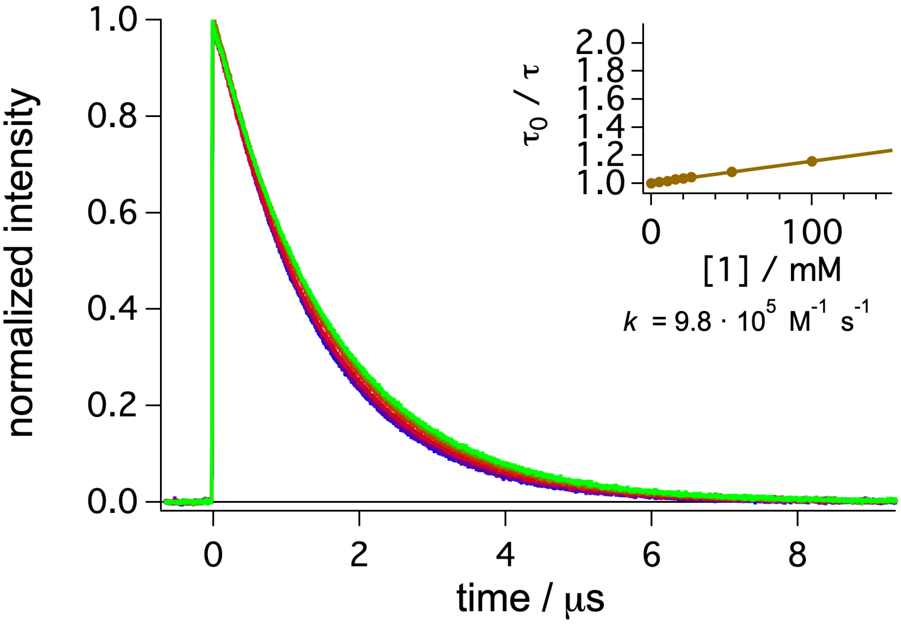

Figure S16. Fluorescence quenching of *fac*-[Ir(ppy)$_3$] by substrate **1**. *fac*-[Ir(ppy)$_3$] (10 µM) in de-aerated DMF was excited at 450 nm and the emission decay was monitored at 515 nm in the absence (green) and in the presence of different concentrations of substrate **1** (5, 10, 15, 20, 25, 50, 100 mM). The Stern-Volmer plot obtained from this data set and the resulting quenching rate constant are given in the inset.

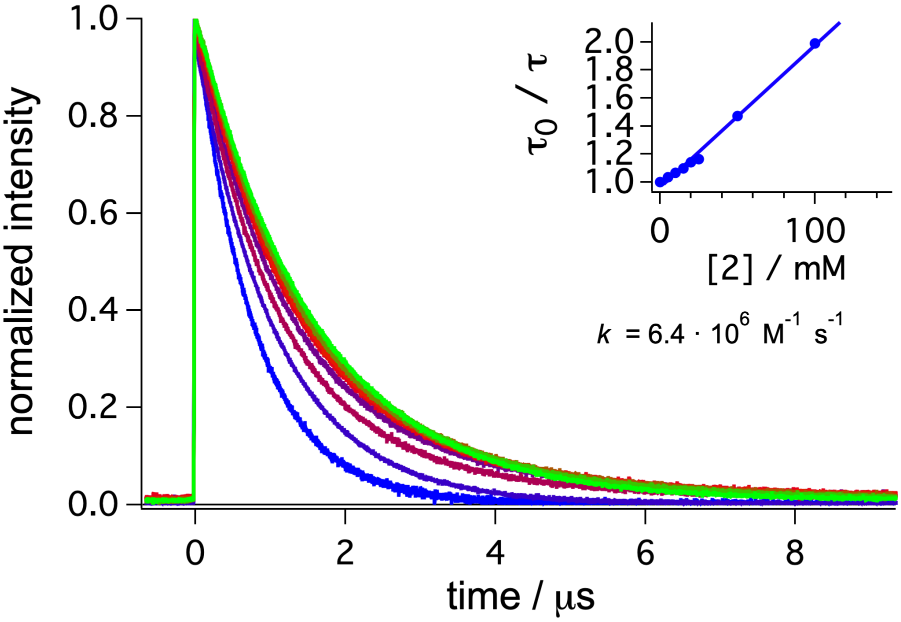

Figure S17. Fluorescence quenching of *fac*-[Ir(ppy)$_3$] by substrate **2**. *fac*-[Ir(ppy)$_3$] (10 µM) in de-aerated DMF was excited at 450 nm and the emission decay was monitored at 515 nm in the absence (green) and in the presence of different concentrations of **2** (5, 10, 15, 20, 25, 50, 100 mM). The Stern-Volmer plot obtained from this data set and the resulting quenching rate constant are given in the inset.

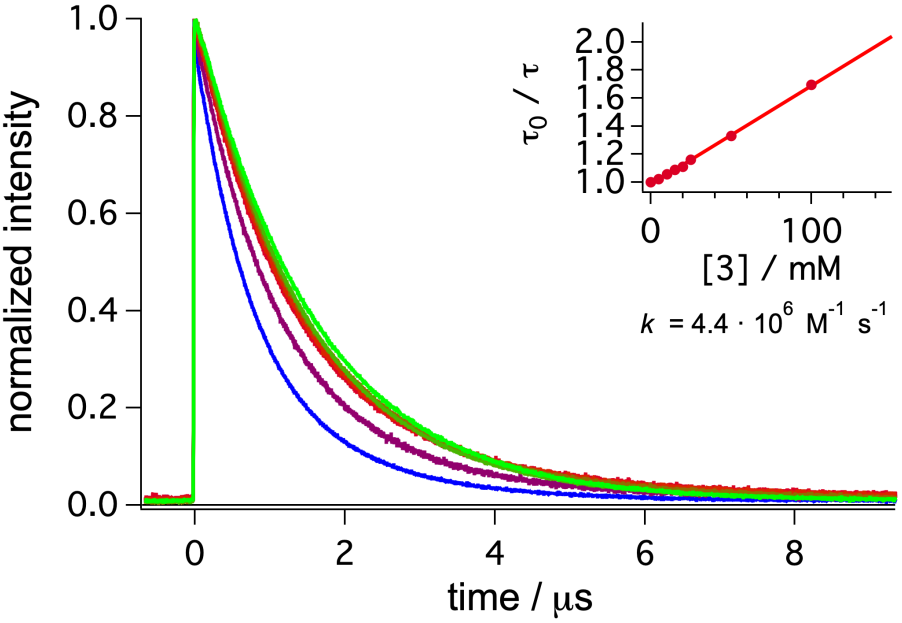

Figure S18. Fluorescence quenching of *fac*-[Ir(ppy)$_3$] by substrate **3**. *fac*-[Ir(ppy)$_3$] (10 μM) in de-aerated DMF was excited at 450 nm and the emission decay was monitored at 515 nm in the absence (green) and in the presence of different concentrations of **3** (5, 10, 15, 20, 25, 50, 100 mM). The Stern-Volmer plot obtained from this data set and the resulting quenching rate constant are given in the inset.

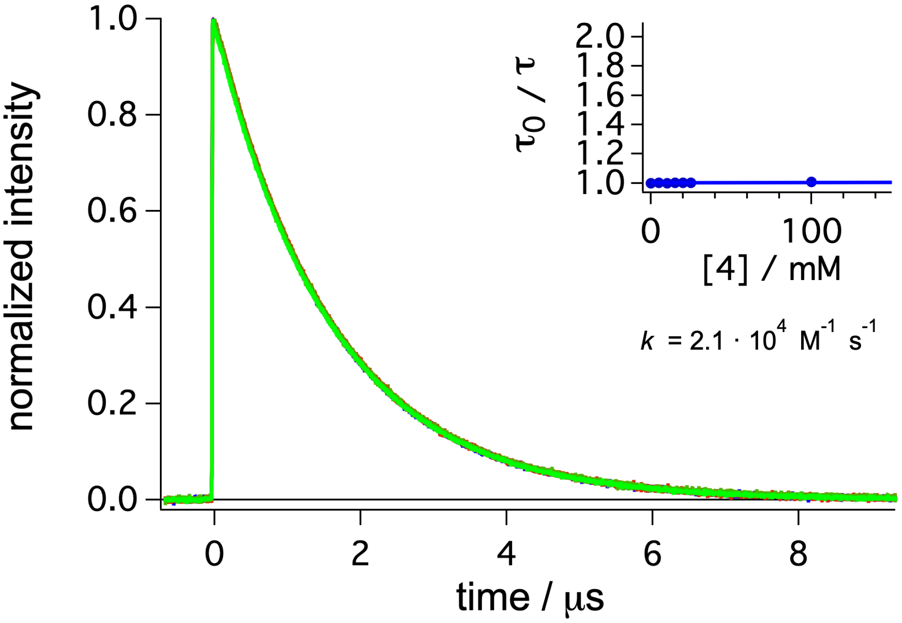

Figure S19. Fluorescence quenching of *fac*-[Ir(ppy)$_3$] by substrate **4**. *fac*-[Ir(ppy)$_3$] (10 μM) in de-aerated DMF was excited at 450 nm and the emission decay was monitored at 515 nm in the absence (green) and in the presence of different concentrations of **4** (5, 10, 15, 20, 25, 100, 250 mM). The Stern-Volmer plot obtained from this data set and the resulting quenching rate constant are given in the inset.

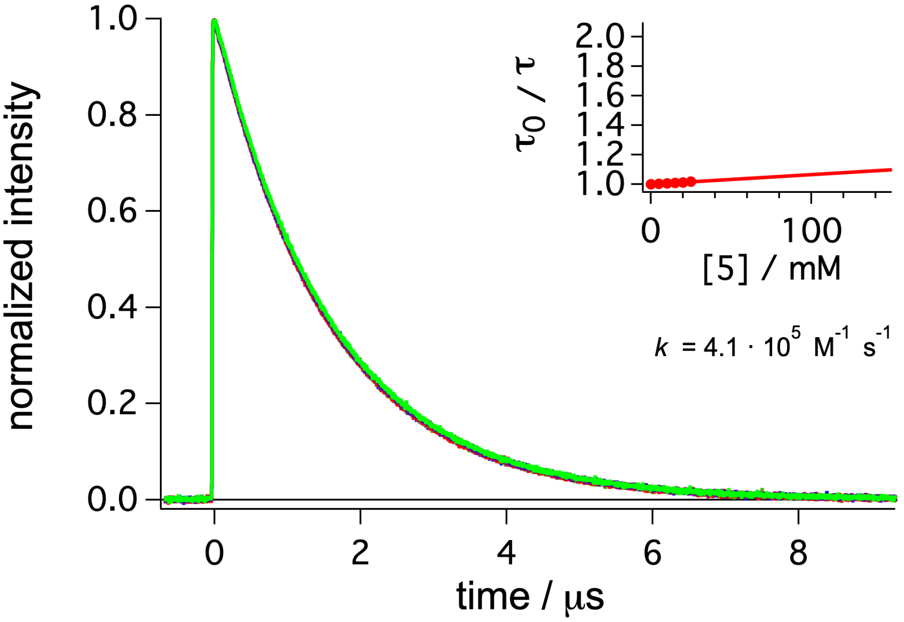

Figure S20. Fluorescence quenching of *fac*-[Ir(ppy)$_3$] by substrate **5**. *fac*-[Ir(ppy)$_3$] (10 µM) in de-aerated DMF was excited at 450 nm and the emission decay was monitored at 515 nm in the absence (green) and in the presence of different concentrations of **5** (5, 10, 15, 20, 25 mM). The Stern-Volmer plot obtained from this data set and the resulting quenching rate constant are given in the inset.

2.9. Direct observation of pyrenyl radical anion under upconversion conditions

We seeked for direct evidence for the formation of pyrenyl radical anion ($^{tBu}Py^{\bullet -}$) under upconversion conditions by transient absorption spectroscopy to further support our mechanistic hypothesis.

In line with the results of section 2.2, excitation of *fac*-[Ir(ppy)$_3$] (10 µM) at 450 nm in de-aerated DMF in the presence of ^{tBu}Py (5 mM) results in a rapid formation of ^{3*tBu}Py with its characteristic peaks at 416 nm and 525 nm in the transient absorption spectra (**Figure S21**A). For a sample containing 10 mM DMA and identical concentrations of *fac*-[Ir(ppy)$_3$] and ^{tBu}Py as before, identical spectroscopic features are visible in the transient absorption spectra (**Figure S21**B). On the other hand, also the relative intensitiy of a signal around 495 nm is increased in comparison to the data without sacrifical electron donor, especially at long delay times. Substraction of the transient absorption spectra recorded 100 µs after the laser pulse in the absence and presence of DMA reveals the formation of a new species with a maximum around 495 nm (the difference of difference spectrum is given in Figure 3C of the main manuscript).[17] By comparison to electrochemically reduced ^{tBu}Py (Figure 3D of the main manuscript) this species can be assigned to the pyrenyl radical anion. This new transient absorption band at 495 nm furthermore manifests in different kinetic traces when monitoring at 495 nm and 416 nm (**Figure S21** C and D). The latter does not change upon addition of DMA, while the traces at 495 nm differ significantly. These results are in line with our proposed mechanism (Figure 2 of the main manuscript). During the formation of the pyrenyl radical anion, an oxidized DMA radical cation is formed and should be visible in the transient absorption spectra, but the extinction coefficient of this unstable intermediate is small ($\varepsilon \approx 2000$ M^{-1} cm^{-1} around 450 nm)[18] compared to the very strongly absorbing pyrenyl radical anion ($\varepsilon \approx 10000$ M^{-1} cm^{-1} around 450 nm) and therefore escapes detection.[17,19,20]

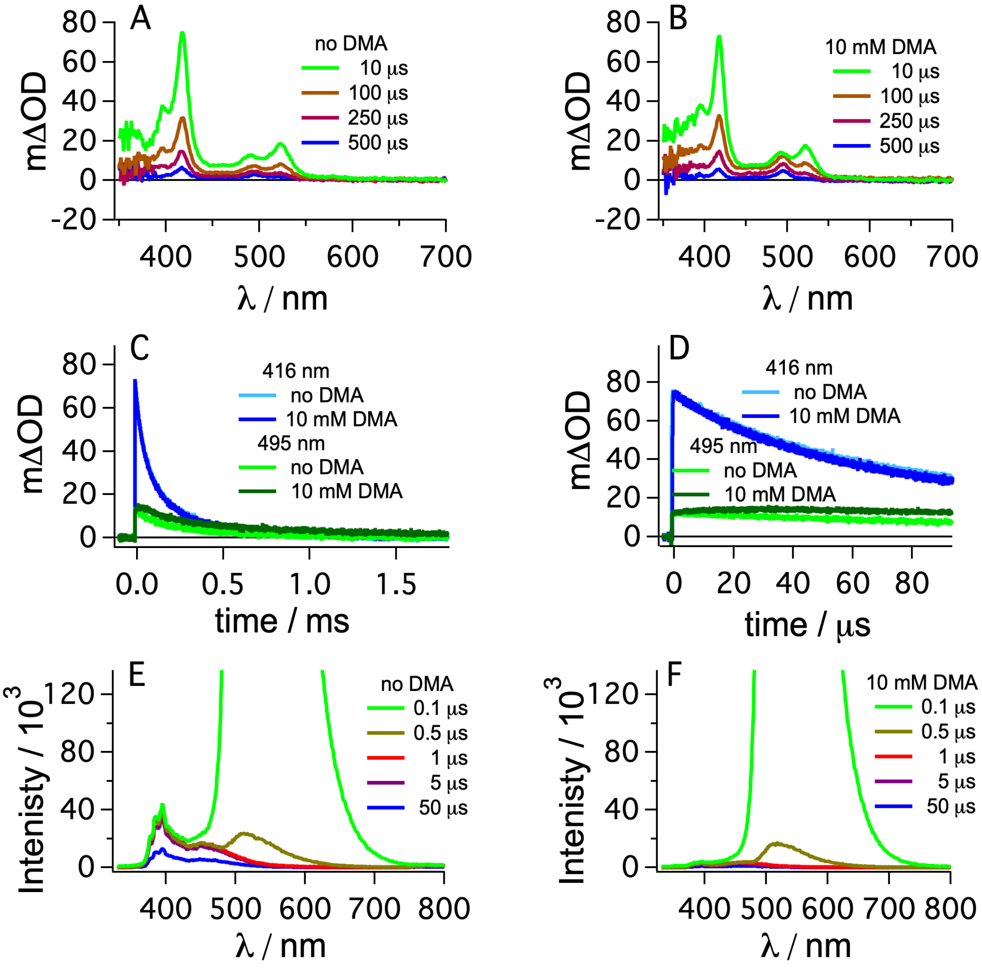

Figure S21. Spectroscopic investigation of pyrenyl radical anion formation under upconversion conditions. Transient absorption spectra of *fac*-[Ir(ppy)$_3$] (10 µM) and ^{tBu}Py (5 mM) in DMF in the absence (A) and in the presence (B) of DMA (10 mM) with different time delays (see inset) after the excitation laser pulses (time-integrated over 200 ns). Kinetic traces over 1.8 ms (C) and 90 µs (D) monitoring the transient absorption signals at 416 nm and 495 nm. Delayed ^{1*tBu}Py emission recorded in absence (E) and in presence of (F) DMA with different time delays (see inset) time-integrated over 200 ns. Pulsed laser excitation at 450 nm was used for all measurements. Further explanations are given in the text.

DMA quenches ^{1*tBu}Py reductively. This is evident in the emission spectra recorded with different time delays after the laser pulse. Upon excitation of the same samples mentioned above in the absence of DMA, the upconverted emission of ^{1*tBu}Py with a maximum around 395 nm is observable (**Figure S21**E), in addition to the (much more intense) prompt emission from the *fac*-[Ir(ppy)$_3$] complex. In contrast to this, for the sample with excess of DMA the upconversion emission band is not visible anymore (**Figure S21**F). This further supports the mechanistic proposal of upconversion (step 1 and 2 in Figure 2 of the main manuscript) followed by reductive quenching of ^{1*tBu}Py (step 3 in Figure 2 of the main manuscript).

In the difference of difference spectrum of Figure 3C in the main paper, a ΔΔOD value of roughly 0.005 is observable for the ^{tBu}Py$^{\bullet-}$ signal at 495 nm. Based on an extinction coefficient of ~10^5 M^{-1} cm^{-1} for the (unsubstituted) pyrenyl radical anion at 495 nm,[21] we estimate a concentration of $5\cdot10^{-8}$ M for ^{tBu}Py$^{\bullet-}$ in the data set of Figure 3C. This concentration is roughly 40 times smaller than the concentration of ^{3*tBu}Py estimated from Figure 3A, where the ΔOD value at 416 nm is 0.08 and the relevant extinction coefficient is ~$4\cdot10^4$ M^{-1} cm^{-1} (estimated from the extinction coefficient of pyrene),[11] leading to a concentration of $2\cdot10^{-6}$ M for ^{3*tBu}Py. Taking into consideration that two ^{3*tBu}Py are needed for the formation of one ^{tBu}Py$^{\bullet-}$, the remaining factor-of-20 difference is explained as follows: (1) Even under optimized conditions, the quantum yield for sTTA-UC ($\phi_{\text{sTTA-UC}}$) amounts to only 0.048. (2) The cage escape yield for the formation of ^{tBu}Py$^{\bullet-}$ and DMA$^{\bullet+}$ from ^{3*tBu}Py is expected to be significantly below 1.0, because geminate recombination of the ^{tBu}Py$^{\bullet-}$ / DMA$^{\bullet+}$ radical pairs is spin-allowed in this case.[22]

2.10. Substrate activation by pyrenyl radical anion

Further information for the results corresponding to step 4 in Figure 2 of the main manuscript is given here.

The very high extinction coefficient of the radical anion of pyrenes around 495 nm offers the possibility to monitor the activation of the substrate.[17] For these experiments, we investigated the decay of the ^{tBu}Py radical anion signal and combined the results of the kinetic data with the information extractable from transient absorption measurements.

The key data and interpretations for the substrate activation by the pyrenyl radical anion are discussed in the main manuscript (Figure 5). Biexponential fit functions for the kinetic decay at 495 nm combined with transient absorption spectra recorded at different delay times are employed to determine the decay time of pyrenyl radical anion in the absence and the presence of substrate **1**, and to estimate the rate constant for electron transfer from ^{tBu}Py$^{\bullet-}$ to substrate **1**.

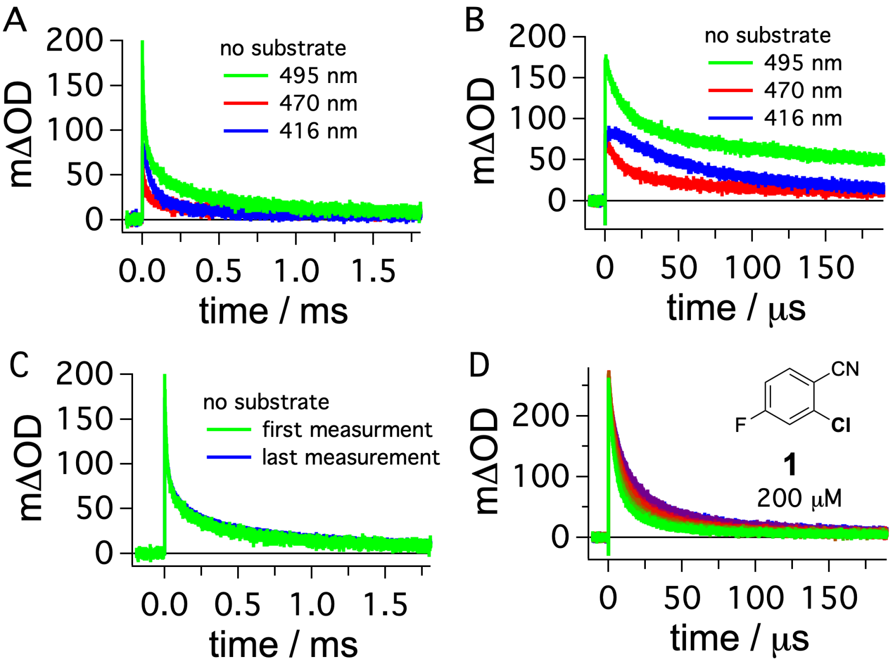

Figure S22. Spectroscopic investigation of substrate activation. Kinetic traces at 495 nm, 470 nm, and 416 nm for ^{tBu}Py (50 µM) in DMF excited at 355 nm in the presence of DMA (10 mM) on a millisecond time scale (A) and with a focus on the first 180 microseconds (B). For measurements in the absence of substrate **1**, no changes are visible for the kinetic decay curves at 495 nm before and after the acquisition of a full set of transient absorption data with about 50 scans in total (C). In the presence of substrate **1** under otherwise identical conditions, the kincetic decay at 495 nm clearly changes rapidly as a function of irradiation time, due to substrate consumption (in this case, each trace consists of 5 repetitions and 10 continuous measurements on the same sample are shown here). Further details are discussed in the text.

Excitation of ^{tBu}Py (50 µM) in de-aerated DMF at 355 nm in the presence of DMA (10 mM) results in the formation of the pyrenyl radical anion (Figure 5A of the main manuscript). The kinetic traces at 495 nm (the main absorption band of ${}^{tBu}\mathrm{Py}^{\bullet -}$) and 470 nm compared to 416 nm (the main absorption band of ^{3*tBu}Py) over the first hundred microseconds (**Figure S22**A and B) are clearly different. The pyrenyl radical anion absorbs at all three wavelengths (see **Figure S23**), but is not the only species contributing to the transient absorption spectra over time. The transient absorption signal at 416 nm (blue trace in **Figure S22**A and B) has a different temporal evolution over the first 180 µs than the signals at 495 / 470 nm (green and red traces in **Figure S22**A and B), pointing towards a process that is happening after the formation of pyrenyl radical anion (the formation of which should be completed within the nanosecond time range, see **Figure S10**). To explain these differences, we consider two options: (I) direct intersystem crossing of ^{tBu}Py and (II) exciplex charge recombination. The intrinsic intersystem efficiency (37 % for unsubstituted pyrene in cyclohexane) is assumed to be less important, as under the relevant conditions (10 mM sacrificial electron donor) about 90 % of ^{1*tBu}Py are quenched by DMA (calculated based on equation S4).[23] Exciplex formation with a sacrificial electron donor (such as DMA),[24] and charge recombination can lead to triplet state formation on microsecond time scales, which could explain the different temporal evolution of the signal at 416 nm (blue trace in **Figure S22**A and B) compared to the signals at 495 nm (green trace) and 470 nm (red trace).[25] As discussed briefly in the main manuscript, protonation of the radical anion is furthermore possible,[17,26] and the DMA radical cation absorbs between 400 nm and 550 nm, though with a comparably low extinction coefficient of $\varepsilon \approx 2000\ M^{-1}\ cm^{-1}$ around 450 nm.[18] All these processes can contribute to the transient absorption kinetics, for example to the kinetic trace recorded at 416 nm and may explain the unusual behaviour seen in the blue trace of Figure S22A and B. These processes can further complicate the analysis of the kinetic traces at 495 nm (near the main absorption band of $^{tBu}Py^{\bullet -}$). Nevertheless, based on the transient absorption spectra in Figure 5A/B, $^{tBu}Py^{\bullet -}$ is the dominant species. This opens the possibility to perform a more detailed analysis of the substrate activation step.

$$\frac{\tau_0}{\tau} = 1 + k_Q \cdot [Q] \cdot \tau_0 \qquad \textbf{(S3)}$$

A Stern-Volmer analysis (equation S3) is commonly used to estimate rate constants for bimolecular reactions, but a direct use of this equation is prevented by the biexponential decay of the kinetic traces at 495 nm. However, the transient absorption spectra in Figure 5A and B of the main manuscript can be used to identify which one of the two decay constants belongs to $^{tBu}Py^{\bullet -}$. In the absence of substrate, biexponential fits yield time constants of 1.07 ms (44%) and 54.7 μs (56%). The transient absorption spectra in Figure 5A reveal that the diagnostic spectral feature of $^{tBu}Py^{\bullet -}$ at 495 nm decreases markedly over the first 50 μs, but remains clearly detectable even after a delay time of 1 ms. Consequently, the two decay times recordable in absence of substrate are both attributed to $^{tBu}Py^{\bullet -}$, but reflect the disappearance of this species via two different mechanistic paths. Taking into account the complexity of the overall system and the number of possible processes in this reaction mixture, a multi-exponential decay of this radical anion intermediate is not overly surprising.

For the measurements in the presence of substrate **1** the data set is somewhat easier to analyze, as the long-lived component (e.g. 28.9 μs (21%) in the presence of 200 μM substrate **1**, inset of Figure 5B) does clearly not correspond to the pyrenyl radial anion based on the transient absorption spectra (Figure 5B). Therefore the faster decay time is used as proxy for the decay time of $^{tBu}Py^{\bullet -}$ in this case. Stern-Volmer analyses were consequently performed using exclusively the faster of the two decay components recordable in presence of substrate. Regardless of whether a value of 1.07 ms or a value of 54.7 μs was employed as τ_0-value in these Stern-Volmer analyses, a rate constant of roughly $1.1 \cdot 10^9\ M^{-1}\ s^{-1}$ was obtained for the reaction of $^{tBu}Py^{\bullet -}$ with substrate **1**. (The data set in Figure 5C of the main manuscript is based on a decay time τ_0 of 1.07 ms; the Stern-Volmer plots based on τ_0 = 54.7 μs is not shown). When performing an identical experiment with DiPEA (instead of DMA) as sacrificial electron donor, a rate constant of $1.5 \cdot 10^9\ M^{-1}\ s^{-1}$ was obtained (data not shown). This result is in good agreement with the data obtained with DMA.

The recording of transient absorption spectra and kinetic measurements with the solution containing ^{tBu}Py and DMA but no substrate **1** (Figure 5A) is unproblematic. The kinetic traces before and after a full set of transient absorption measurements (as provided in Figure 5A) are identical (**Figure S22**C), indicating high reversibility of all photoinduced processes occurring in this mixture. In clear contrast to that, the mixture containing ^{tBu}Py, DMA, and substrate **1** can undergo irreversible photoinduced processes (due to substrate turnover), and this complicates the recording of transient absorption spectra and kinetic traces. The kinetic traces clearly change significantly already in the presence of only small concentrations of substrate **1** with an increasing number of excitation events (presumably because of a change in substrate concentration with increasing number of laser pulses), as seen for example from **Figure S22**D. Therefore, the data collection for kinetic traces and transient absorption spectra in Figure 5B and **Figure S22** were performed with maximum of two scans for each data set and a maximum of two data sets for transient absorption measurements with each sample that contained substrate **1**. Kinetic data presented in the main paper has been limited to acquisition times up to 180 μs to simplify a graphical comparison, but the exact decay constants in the absence of substrate **1** were obtained from measurements on a millisecond time range (**Figure S22**C).

2.11. Quenching efficiencies of all relevant steps including substrate activation

Quenching efficiencies are calculated by the following equation:

$$\eta = 1 - \frac{\tau}{\tau_0} \qquad \textbf{(S4)}$$

Using the experimentally determined rate constants for the individual steps, the decay times of the individual excited or radical species under catalytic conditions can be calculated (assuming pseudo first-order decay behaviour in the case of ^{tBu}Py$^{\bullet-}$). This is done based on the Stern-Volmer equation (equation S5) resulting in an equation for the decay time τ (equation S6), which is dependent on the specific rate constant k_Q and concentration of the respective quencher Q.

$$\frac{\tau_0}{\tau} = 1 + k_Q \cdot [Q] \cdot \tau_0 \qquad \textbf{(S5)}$$

$$\tau = \left(\frac{1}{\tau_0} + k_Q \cdot [Q]\right)^{-1} \qquad \textbf{(S6)}$$

The efficiencies are calculated for the conditions at the beginning of the photocatalytic reaction of substrate **1** (conditions: 30 mM **1**, 1 mol% *fac*-[Ir(ppy)$_3$], 10 mol% ^{tBu}Py, 5 eq. DMA). Efficiencies (η) are summarized in

Table S4 and a more detailed overview of all relevant data for the respective calculations of η follows afterwards (text and **Table S5**).

Table S4. Efficiencies (η) for the individual elementary processes illustrated in Figure 2 of the main manuscript. All values for de-aerated DMF at 20 °C.

step no.	description of step	η [a]	more information to this step in section
1	TTET from *fac*-[Ir(ppy)$_3$] to ^{tBu}Py	0.91	2.2
1b	reductive quenching of *fac*-[Ir(ppy)$_3$] by DMA	0.003	2.3
1c	oxidative quenching of *fac*-[Ir(ppy)$_3$] by substrate **1**	0.05	2.8
2	TTA-UC of ^{tBu}Py	0.99 [b]	2.5
2b	reductive quenching of ^{3*tBu}Py by DMA	<0.05	2.4
3	reductive quenching of ^{1*tBu}Py by DMA	0.99	2.6
3b	oxidative quenching of ^{1*tBu}Py by substrate **1**	0.31	2.7
4	electron transfer from ^{tBu}Py$^{\bullet-}$ to substrate **1**	0.99	2.10

(a) Efficiencies estimated based on the initial concentrations in the photocatalytic reactions (substrate **1** (30 mM), *fac*-[Ir(ppy)$_3$] (1 mol%), ^{tBu}Py (10 mol%) and DMA (5 eq.)). This table is also given in the main manuscript (Table 2). An overview for the values used to calculate the efficiencies is provided in **Table S5**.

Table S5. Detailed overview of reactive species, quencher (Q) and their concentrations ([Q]), rate constants (k), unquenched (τ_0) and calculated quenched decay times (τ) and the efficiencies (η) for the individual elementary processes illustrated in Figure 2 of the main manuscript.

step no.	reactive species	τ_0 / ns	Q	[Q] / mM	k / M^{-1} s^{-1}	τ / ns [a]	η [b]
1	*fac*-^{3*}[Ir(ppy)$_3$]	1590	^{tBu}Py	3	$2.1 \cdot 10^{9}$	144	0.91
1b	*fac*-^{3*}[Ir(ppy)$_3$]	1590	DMA	150	$1.1 \cdot 10^{4}$	1586	0.003
1c	*fac*-^{3*}[Ir(ppy)$_3$]	1590	**1**	30	$9.8 \cdot 10^{5}$	1519	0.05
2	^{3*tBu}Py	335000	^{3*tBu}Py	0.027 [c]	$1.1 \cdot 10^{10}$	3301	0.99 [b]
2b	^{3*tBu}Py	335000	DMA	150	$<1.0 \cdot 10^{3}$	>319000	<0.05
3	^{1*tBu}Py	235	DMA	150	$4.8 \cdot 10^{9}$	1	0.99
3b	^{1*tBu}Py	235	**1**	30	$6.4 \cdot 10^{7}$	162	0.31
4	^{tBu}Py$^{\bullet-}$	1070000	**1**	30	$1.1 \cdot 10^{9}$	162	0.99

All calculations are based on the initial concentrations in the photocatalytic reactions (substrate **1** (30 mM), *fac*-[Ir(ppy)$_3$] (1 mol%), ^{tBu}Py (10 mol%) and DMA (5 eq.)) unless otherwise noticed. (a) The quenched decay times are calculated with equation S6. (b) Efficiencies are calculated with equation S4. (c) Estimation of this concentration is discussed in further detail in the text.

A list of the reactive species with the individual natural decay times (τ_0) as well as the relevant quencher for each elementary step is in **Table S5**. Together with the rate constant (k) and the concentration of each quencher, equation S6 is applied to calculate the resulting quenched decay time (τ) under photocatalytic conditions.

Rate constants for step 1, 1b, 1c, 3 and 3b are obtained from Stern-Volmer emission quenching studies for excited photocatalysts with a mono-exponential decay and the quenching efficiencies can be calculated in straightforward fashion using equation S6. In step 2, two $^{3*\mathrm{tBu}}$Py molecules undergo triplet-triplet annihilation upconversion. Consequently, $^{3*\mathrm{tBu}}$Py serves also as quencher in this step and an estimation of its concentration is required under catalytic conditions. For a rough estimation we make several assumptions: First of all, we we assume that per photoexcited *fac*-[Ir(ppy)$_3$] only one equivalent of $^{3*\mathrm{tBu}}$Py is formed. (Based on the much longer lifetime of $^{3*\mathrm{tBu}}$Py and due to the fact that $^{\mathrm{tBu}}$Py is present in tenfold higher concentration than *fac*-[Ir(ppy)$_3$], each photoexcited *fac*-[Ir(ppy)$_3$] complex could in principle sensitize several $^{\mathrm{tBu}}$Py molecules, before $^{3*\mathrm{tBu}}$Py decay has occurred). In the upconversion quantum yield experiment (Figure 4 of the main manuscript), saturation is achieved under laser cw-excitation above 2 W cm^{-2}, indicating that near this threshold power density our upconversion system begins to operate in the so-called strong annihilation limit. The photoredox catalysis was performed using cw-laser irradiation with a power density of about 42.5 W cm^{-2}, and consequently it seems plausible that under these conditions, too, the upconversion operates in the strong annihilation limit. Using the calculated efficiency of 0.909 for the triplet-triplet energy transfer and an initial concentration of 0.3 mM of *fac*-[Ir(ppy)$_3$] under catalytic conditions, we obtain a concentration of 0.27 mM for $^{3*\mathrm{tBu}}$Py. Using this concentration and a quenching constant of $1.1 \cdot 10^{10}$ M^{-1} s^{-1}, equation S4 results in a quenching efficiency of 0.999. Given the crude assumptions made above, it is likely that the initial $^{3*\mathrm{tBu}}$Py concentration is overestimated. However, for a ten times lowered $^{3*\mathrm{tBu}}$Py concentration (27 µM) one still obtains an annihilation efficiency of 0.990 for step 2. A value of 0.99 is used in Table 2 for this step.

Although the quenching efficiency can give insight into the individual steps of our catalytic cycle, a direct comparison of the calculated efficiencies in Table S5 can be misleading. The more important quantity to compare the importance of two potentially competing processes is the product of the rate constant (k_Q) and the quencher concentration ([Q]), resulting in an estimation of the number of reaction events per unit time. As noted in the main manuscript, this simple analysis shows that reductive quenching of $^{1*\mathrm{tBu}}$Py by DMA (step 3 in Figure 2) is faster by a factor of ca. 400 compared to oxidative quenching of $^{1*\mathrm{tBu}}$Py by substrate **1** (step 3b in Figure 2).

2.12. Spectro-electrochemical characterization of pyrenyl radical anion

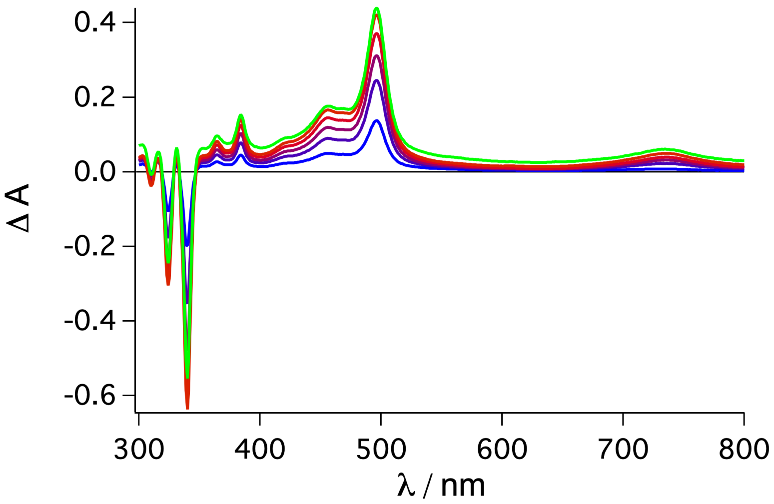

Figure S23. UV-Vis difference spectrum obtained upon electrochemical reduction of ^{tBu}Py in de-aerated DMF with an applied potential of -2.25 V *vs* SCE in the presence of TBAPF$_6$ (0.1 M) as supporting electrolyte. The green trace of this dataset is also displayed in Figure 3D of the main manuscript.

A spectro-electrochemical reduction of a solution containing ^{tBu}Py (1 mM) and TBAPF$_6$ (0.1 M) as supporting electrolyte in de-aerated DMF with an applied potential of -2.25 V *vs* SCE resulted in a bleach of the ground state absorbance of ^{tBu}Py (negative signals below 350 nm) as well as the growth of new absorption bands with maxima at 496 nm and 456 nm (**Figure S23**). The spectra in Figure S23 are in line with previously published spectra for pyrenyl radical anion.[17]

2.13. Cyclic voltammetry of catalytic system components and substrates

Cyclic voltammetry was performed with a saturated calomel electrode (SCE) as reference electrode, a glassy carbon disk as working electrode, and a silver wire as counter electrode. Measurements were conducted with potential sweep rates of 0.1 V/s in dry de-aerated DMF containing 0.1 M TBAPF$_6$ as an electrolyte. For oxidations or reductions with irreversible waves, peak potentials are reported. Cyclic voltammetry measurements are presented for *fac*-[Ir(ppy)$_3$] and ^{tBu}Py (**Figure S24**) as well as for substrates **1** to **5** (**Figure S25**), while the corresponding oxidation and reduction potentials are summarized in **Table S6**.

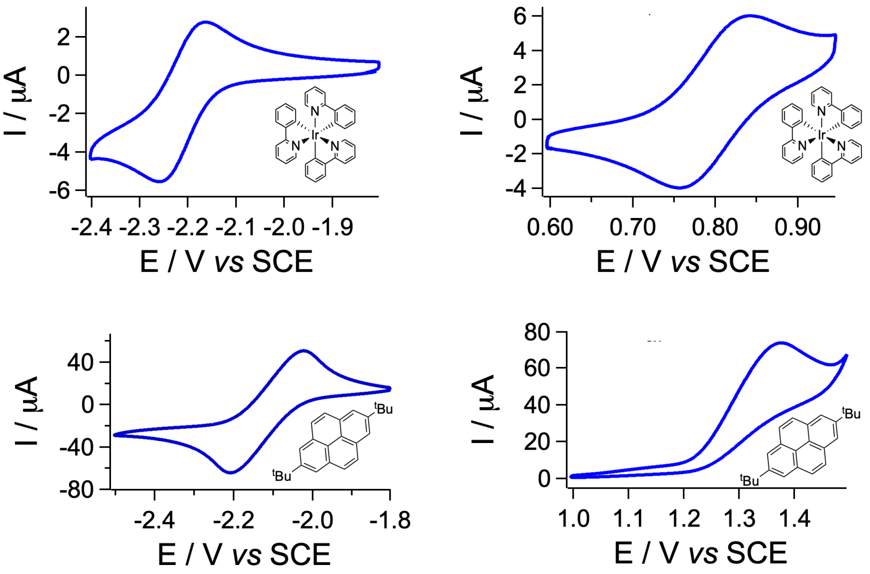

Figure S24. Cyclic voltammetry measurements of catalytic system components determined with $TBAPF_6$ (0.1 M) as supporting electrolyte in de-aerated DMF. Voltammograms were recorded with scan rates of 100 mV s^{-1}.

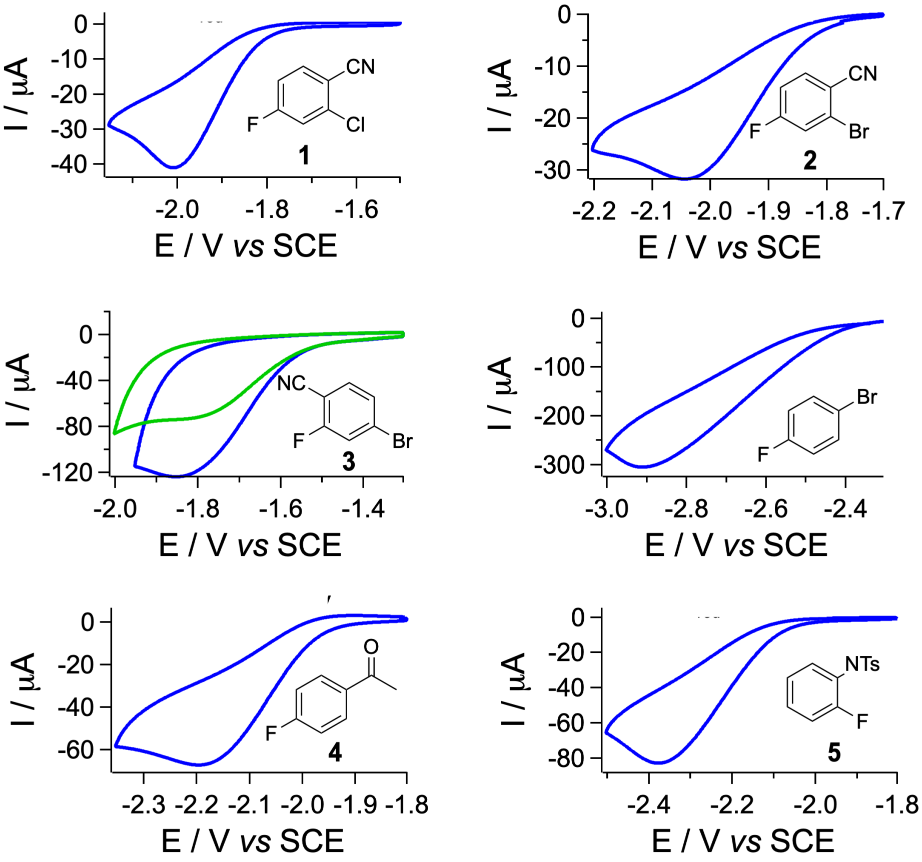

Figure S25. Cyclic voltammetry measurements of substrates determined with $TBAPF_6$ (0.1 M) as supporting electrolyte in de-aerated DMF. Voltammograms were recorded with scan rates of 100 mV s^{-1} (blue) or 50 mV s^{-1} (green).

Table S6. Oxidation and reduction potentials of catalytic system components and substrates in DMF *vs* SCE.

compound	E_{ox} / V *vs* SCE	E_{red} / V *vs* SCE
fac-[Ir(ppy)$_3$]	0.80	-2.20
$^{\mathrm{tBu}}$Py	1.37 [a]	-2.11
2-chloro-4-fluorobenzonitrile (**1**)	- [b]	-2.0 [a]
2-bromo-4-fluorobenzonitrile (**2**)	- [b]	-2.0 [a]
4-bromo-2-fluorobenzonitrile (**3**)	- [b]	~ -1.8 [a]
4-fluoroacetophenone (**4**)	- [b]	-2.2 [a]
N-(2-fluorophenyl)-4-methylbenzenesulfonamide (**5**)	- [b]	-2.4 [a]
1-bromo-4-fluorobenzene	- [b]	-2.9 [a]

Conditions: Measurements in de-aerated DMF with 0.1 M TBAPF$_6$ and a scan rate of 0.1 V s^{-1}. (a) Irreversible oxidation/reduction peak. (b) Not measured.

3. Irradiation setup

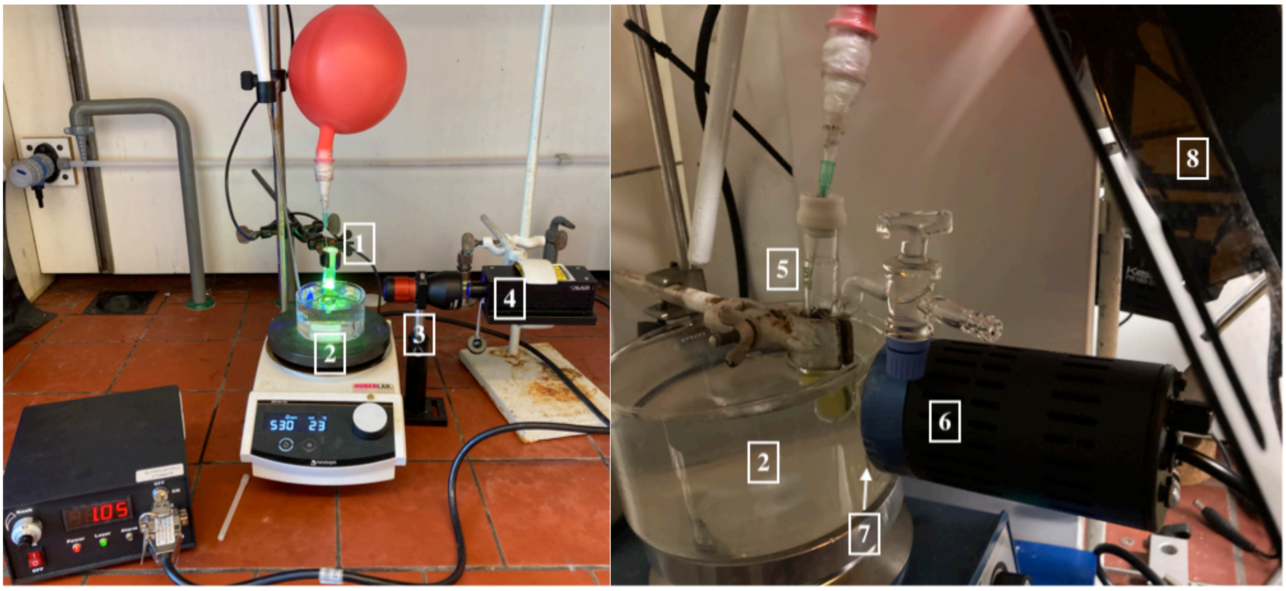

Figure S26. Irradiation setup for photoredox reactions with 447 nm cw laser (left) or 440 nm LED (right). 1: stirred screw-cap quartz cuvette with reaction mixture under argon; 2: stirred water bath for cooling of irradiated solution; 3: beam expander (used backwards) to reduce the size the laser beam; 4: 447 nm cw laser; 5: stirred Schlenk tube with reaction mixture under argon; 6: 440 nm LED; 7: two coloured glass 400 nm cut-off filters; 8: cooling fan.

4. Synthetic procedures and photocatalysis experiments

4.1. General procedures and isolated products

4.1.1. Photocatalytic dehalogenation – General Procedure with 447 nm cw-laser

A quartz cuvette with septum cap was equipped with a magnetic stir bar and charged with substrate (e. g. 90 µmol, 1 eq.), *fac*-[Ir(ppy)$_3$] (e. g. 589 µg, 1 mol%) and 2,7-di(*tert*-butyl)pyrene (e. g. 2.83 mg, 9 µmol, 10 mol%). DMF (3 mL), internal standard (4-fluorotoluene, 9.91 µL, 1 eq.) and *N,N*-dimethylaniline (56 µL, 5 eq.) were added. The solution was purged with argon for at least 7 minutes and a balloon of argon was installed for the duration of the reaction. The stirred solutions were irradiated for specified durations with a 447 nm diode laser (Roithner Lasertechnik, 1070 mW) using a beam expander (Thorlabs, GBE05-A used backwards) to compress the beam. Product formation was monitored by ^{19}F-NMR spectroscopy (0.2 mL of the reaction solution was diluted with 0.4 mL of benzene-d$_6$, before and after irradiation. The conversion and the yield were determined against the internal standard).

4.1.2. Photocatalytic reduction reaction – General Procedure with a 440 nm LED

A Schlenk tube was equipped with a magnetic stir bar and charged with substrate (e. g. 90 µmol, 1 eq.), *fac*-[Ir(ppy)$_3$] (e. g. 589 µg, 1 mol%) and 2,7-di(*tert*-butyl)pyrene (e. g. 2.83 mg, 9 µmol, 10 mol%). DMF (3 mL), internal standard (4-fluorotoluene, 9.91 µL, 1 eq.) and *N,N*-dimethylaniline (56 µL, 5 eq.) were added and the tube was closed with a septum. The solution was purged with argon for at least 7 minutes and a balloon of argon was installed for the duration of the reaction. The stirred solutions were irradiated for specified durations with a 440 nm LED (Kessil PR160, 40 W) and two 400 nm long-pass cut-off filters (Reichman Feinoptik GmbH) were installed in between the lamp and the tube. Product formation was monitored by ^{19}F-NMR spectroscopy (0.2 mL of the reaction solution was diluted with 0.4 mL of benzene-d$_6$ before and after irradiation. The conversion and the yield were determined against the internal standard).

Unlike the laser, the LED has no collimated beam and the position of the LED is therefore expected to have a larger influence on the photoreaction outcome than in the case of the laser. To account for that, not more than two samples were irradiated at once with this setup and all determined yields and conversions were averaged over two independent measurements.

4.2. Confirmation of formed products

All products from photochemical reactions were identified by comparison of their ^{19}F-NMR spectra to those of reference compounds that were either commercially available or that were synthesized in a separate manner.

4.2.1. 2,3-bis(4-fluorophenyl)butane-2,3-diol (4-P)

Following a known procedure,[27] the dimerization of 4-fluoro-acetophenone (**4**) was performed on a 5 mmol scale to obtain 2,3-bis(4-fluorophenyl)butane-2,3-diol as white solid (**4-P**, 61 mg, 9%), comprised of a 1:2 mixture of *meso* and dl isomers.

The ^{1}H-NMR spectra are in line with previously reported data.[28] Assignment of isomers was accomplished following the literature.[28]

dl: **^{1}H{^{19}F}-NMR** (400 MHz, $CDCl_3$): δ 7.14 – 7.10 (m, 4H), 6.96 – 6.86 (m, 4H), 2.49 (s, 2H), 1.49 (s, 6H) ppm.

dl: **^{19}F{^{1}H}-NMR** (376 MHz, $CDCl_3$): δ 115.90 (s, 2F) ppm.

dl: **^{13}C-NMR** (126 MHz, $CDCl_3$): δ 162.15 (d, $^1J_{CF}$ = 246.0 Hz), 139.20 (d, $^4J_{CF}$ = 3.2 Hz), 129.20 (d, $^3J_{CF}$ = 7.9 Hz), 114.06 (d, $^2J_{CF}$ = 21.0 Hz, 2C), 78.73 (s), 25.07 (s) ppm.

meso: **^{1}H{^{19}F}-NMR** (400 MHz, $CDCl_3$): δ 7.22 – 7.16 (m, 4H), 6.96 – 6.86 (m, 4H), 2.25 (s, 2H), 1.57 (s, 6H) ppm.

meso: **^{19}F{^{1}H}-NMR** (376 MHz, $CDCl_3$): δ 116.19 (s, 2F) ppm.

meso: **^{13}C-NMR** (126 MHz, $CDCl_3$): δ 162.05 (d, $^1J_{CF}$ = 245.8 Hz), 139.59 (d, $^4J_{CF}$ = 3.3 Hz), 128.80 (d, $^3J_{CF}$ = 7.9 Hz), 114.14 (d, $^2J_{CF}$ = 21.1 Hz), 78.46 (s), 25.35 (s) ppm.

4.2.2. Isolated yield of 2,3-bis(4-fluorophenyl)butane-2,3-diol (4-P)

A stock solution containing 4-fluoroacetophenone (**4**, 79.6 mg 576 µmol, 1 eq.), *fac*-[Ir(ppy)$_3$] (860 µg, 1.31 µmol, 0.22 mol%), 2,7-di(*tert*-butyl)pyrene (17.0 mg, 54.1 µmol, 9.3 mol%) and *N,N*-dimethylaniline (360 µL, 2.88 mmol, 5 eq.) in DMF (18 mL) was prepared and equal volumes were distributed over six Schlenk tubes. All tubes were capped with a septum; the solutions were purged with argon for at least 7 minutes and a balloon of argon was installed for the duration of the reaction. The stirred solutions were irradiated for 30 min in pairs of two with a 440 nm LED (Kessil PR160, 40 W). Two 400 nm long-pass cut-off filters (Reichmann Feinoptik GmbH) were installed in between the lamp and the tubes. The six reaction mixtures were then combined and the solvent was removed under reduced pressure. The crude product was purified by flash column chromatography (SiO_2, cyclohexane → cyclohexane/ethyl acetate 4:1) to obtain the pure 2,3-bis(4-fluorophenyl)butane-2,3-diol (**4-P**, 54.2 mg, 195 µmol, 68 %) as a mixture of isomers (dl:*meso* 1.06:1).

The spectroscopic data match those obtained through a literature procedure (see above).

As a side-product, 2-(4-fluorophenyl)-1-(methyl(phenyl)amino)propan-2-ol (**4-SP**) has been found and characterized. The yield of this side-product was not determined.

^{1}H{^{19}F}-NMR (400 MHz, $CDCl_3$): δ 7.47 (d, $J_{H,H}$ = 8.9 Hz, 2H), 7.23 (dd, $J_{H,H}$ = 8.9 Hz, $J_{H,H}$ = 7.2 Hz, 2H), 7.05 (d, $J_{H,H}$ = 9.0 Hz, 2H), 6.87 (d, $J_{H,H}$ = 8.7 Hz, 2H), 6.77 (t, $J_{H,H}$ = 7.3 Hz, 2H), 3.58 (d, $J_{H,H}$ = 14.9 Hz, 2H), 3.50 (d, $J_{H,H}$ = 14.9 Hz, 2H), 2.69 (s, 3H), 2.62 (s, 1H), 1.61 (s, 3H) ppm.

^{19}F{^{1}H}-NMR (376 MHz, $CDCl_3$): δ 116.43 (s, 1F) ppm.

^{13}C-NMR (126 MHz, $CDCl_3$): δ 161.98 (d, $^{1}J_{CF}$ = 245.2 Hz), 151.30 (s), 142.72 (d, $^{4}J_{CF}$ = 3.2 Hz), 129.24 (s), 126.81 (d, $^{3}J_{CF}$ = 7.9 Hz), 117.91 (s), 115.19 (d, $^{2}J_{CF}$ = 21.1 Hz), 118.41 (s), 75.06 (s), 66.35 (d, $^{5}J_{CF}$ = 1.0 Hz), 40.42 (s), 28.32 (s) ppm.

4.3. Conversion and product formation over time using a cw-laser

Table S7. Conversion and product formation over time with a 447 nm cw-laser.

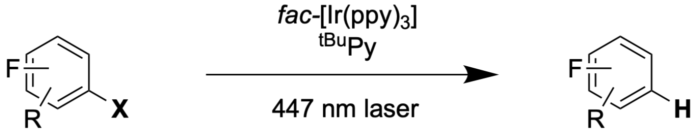

entry	substrate	time / h	yield (conversion) / % [a]	
1[b]	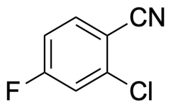 **1**	1	36 (45)	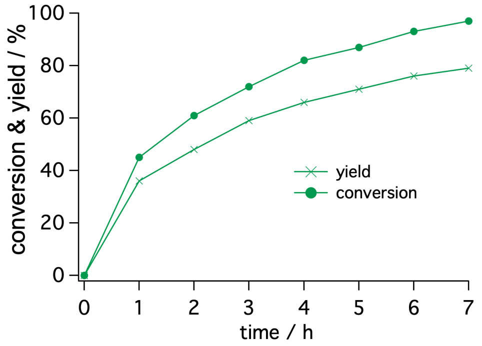
		2	48 (61)	
		3	59 (72)	
		4	66 (82)	
		5	71 (87)	
		6	76 (93)	
		7	79 (97)	
2	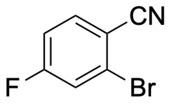 **2**	1	31 (35)	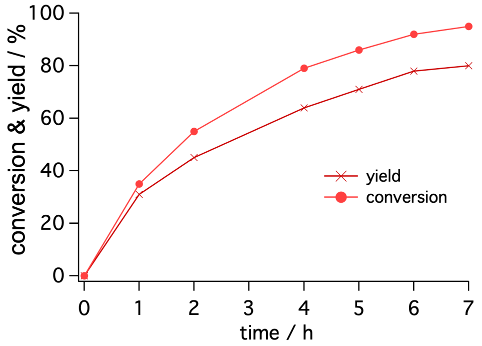
		2	45 (55)	
		4	65 (79)	
		5	71 (86)	
		6	78 (92)	
		7	80 (95)	
3		0.5	23 (31)	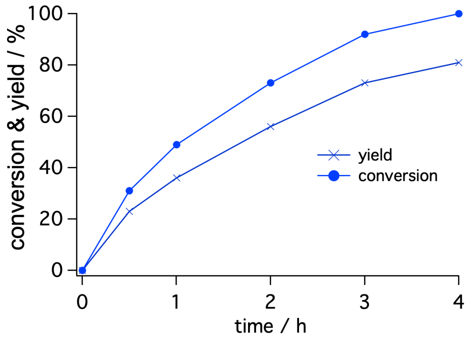
	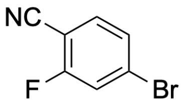 **3**	1	36 (49)	
		2	59 (72)	
		3	76 (92)	
		4	82 (100)	

(a) Reaction conditions identical to those given in the general procedure with a 447 nm cw-laser (section 4.1). (b) Data from entry 1 is also included in the main manuscript (Figure 7).

In the main manuscript, the conversion of substrate **1** (and the yield of product **1-P**) based on ^{19}F-NMR analysis with an internal standard is given over time (see Figure 7). Analogous results for substrates **2** and **3** under cw-laser excitation are presented in **Table S7**.

4.4. Power dependence of product formation with blue LED

The spectroscopic investigations and the catalytic reactions occurred with very different concentrations of substrates, sensitizers and annihilators. Whilst the bi-photonic nature of the SenI-ET process is well established for the spectroscopic experiments (Figure 4D), it seemed meaningful to corroborate this also for the photocatalytic reaction conditions. We have chosen an approach that has been previously employed for bi-photonic photoredox systems.[29,30]

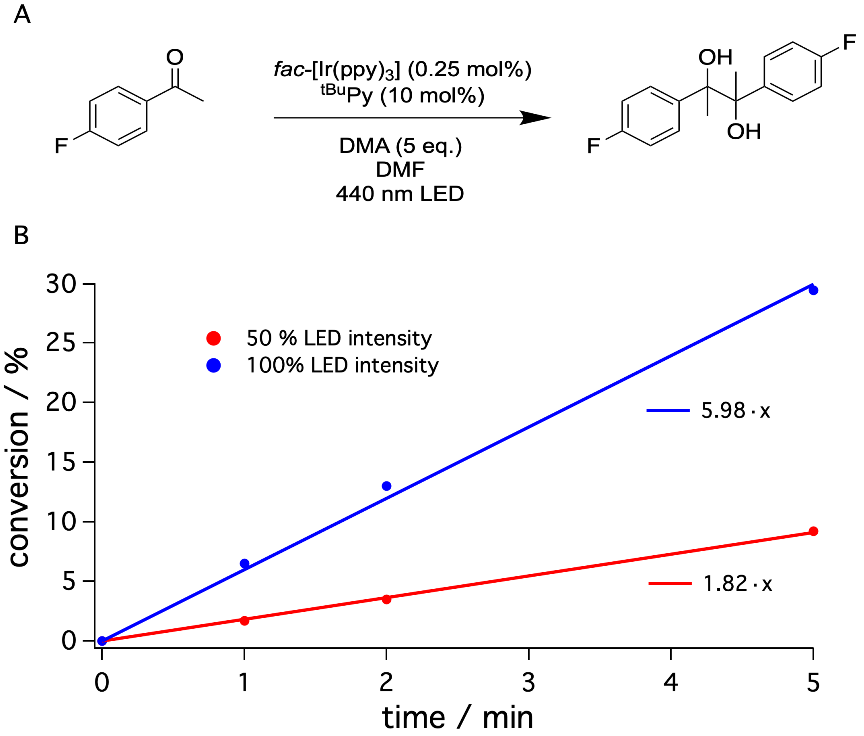

Figure S27. Investigated dimerization reaction for investigation of the power dependence of the SenI-ET process under photocatalytic conditions (A). Conversion of starting material 5 was monitored over time with 50 % and 100 % LED intensity (B). The solid lines are linear regression fits to the experimental data (intercepts set to 0), resulting in the slopes indicated on the right-hand side. Samples were prepared according to the general procedure for irradiation with an LED and analysed by ^{19}F-NMR spectroscopy.

The dimerization of **5** was investigated (**Figure S27**A). This reaction is thermodynamically demanding, because two acetophenone radical anions are needed for a successful product formation. We monitored the conversion of **5** over the first 5 minutes of the reaction with 50 % and 100 % LED intensity (Kessil PR160, 440 nm). In theory for a biphotonic mechanism, a quadratic dependence on the irradiation intensity should be visible (resulting in a quadrupled substrate conversion for a doubled light intensity). Indeed, we found an increase by a factor of 3.3 for the conversion of **5** with a doubled light intensity (resulting from ratio of 5.98 to 1.82 based on the slopes of the linear regression fits in **Figure S27**B), which supports our hypothesis that our investigated mechanism is also present under elevated concentrations compared to the spectroscopic experiments. Deviation from a perfectly quadratic dependence might be due to (partial) catalyst poisoning and a saturation effect at higher concentrations. Nevertheless, our data clearly support a bi-photonic rather than a mono-photonic mechanism.

5. NMR data

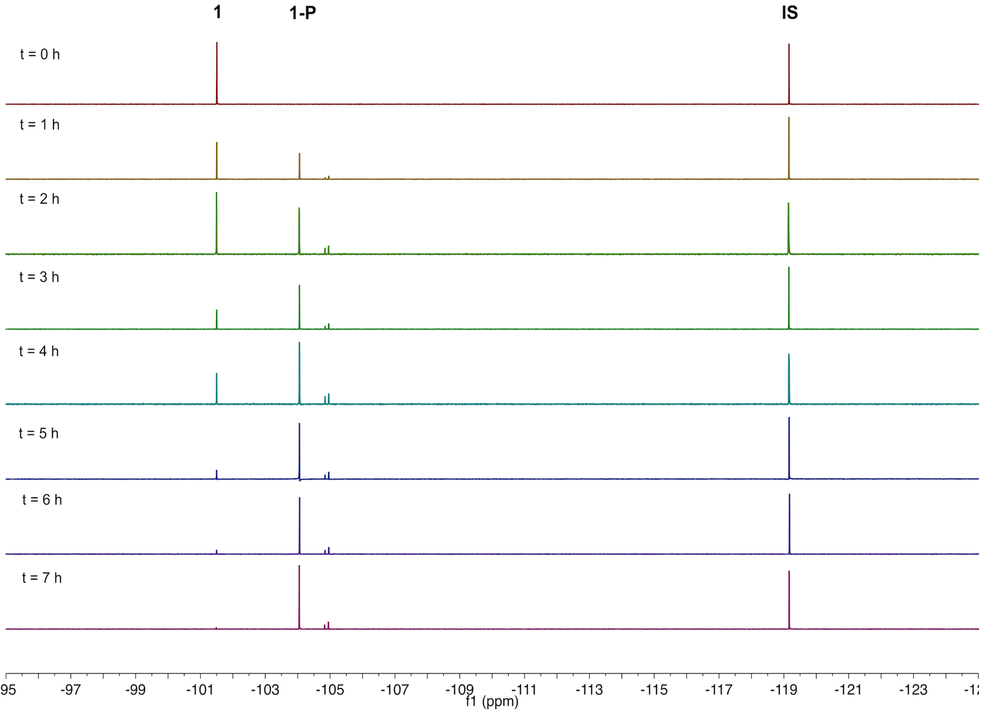

Figure S28. ^{19}F-NMR spectra monitoring dechlorination of substrate **1** over time using 447 nm cw-laser irradiation. Reaction conditions: 30 mM **1**, 1 mol% *fac*-[Ir(ppy)$_3$], 10 mol% ^{tBu}Py and 5 eq. DMA in DMF. IS = internal standard (4-fluorotoluene). Unassigned signals at -104.85 ppm and -104.93 ppm are unidentified side products most likely based on side reactions with DMA related degradation intermediates.

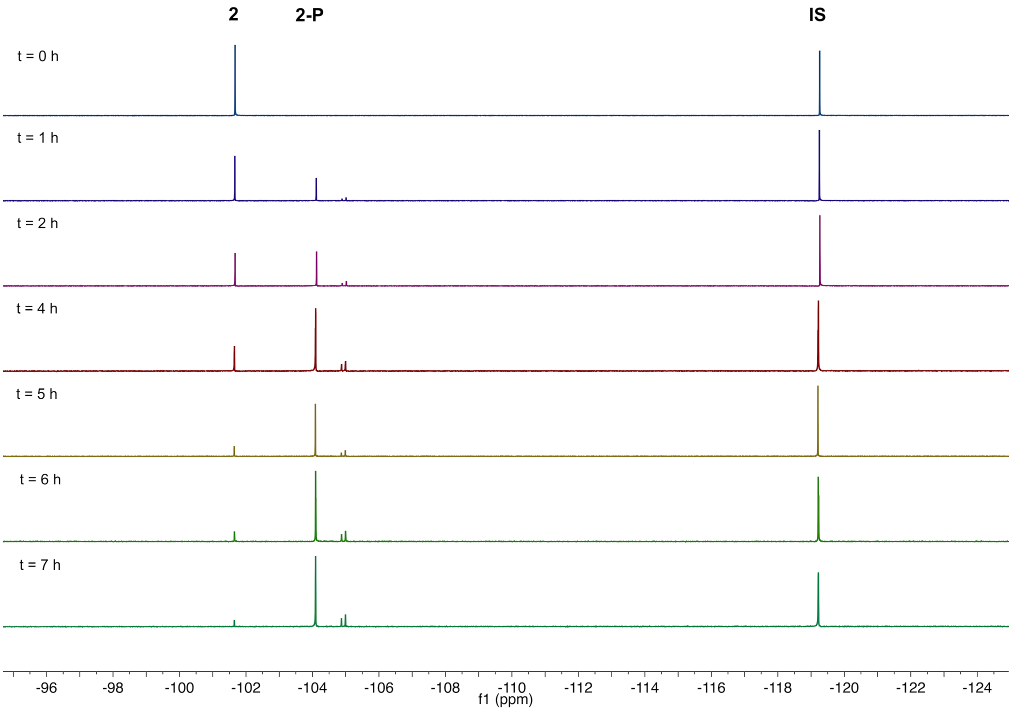

Figure S29. ^{19}F-NMR spectra monitoring debromination of substrate **2** over time using 447 nm cw-laser irradiation. Reaction conditions: 30 mM **2**, 1 mol% *fac*-[Ir(ppy)$_3$], 10 mol% ^{tBu}Py and 5 eq. DMA in DMF. IS = internal standard (4-fluorotoluene). Unassigned signals at -104.85 ppm and -104.93 ppm are unidentified side products most likely based on side reactions with DMA related degradation intermediates.

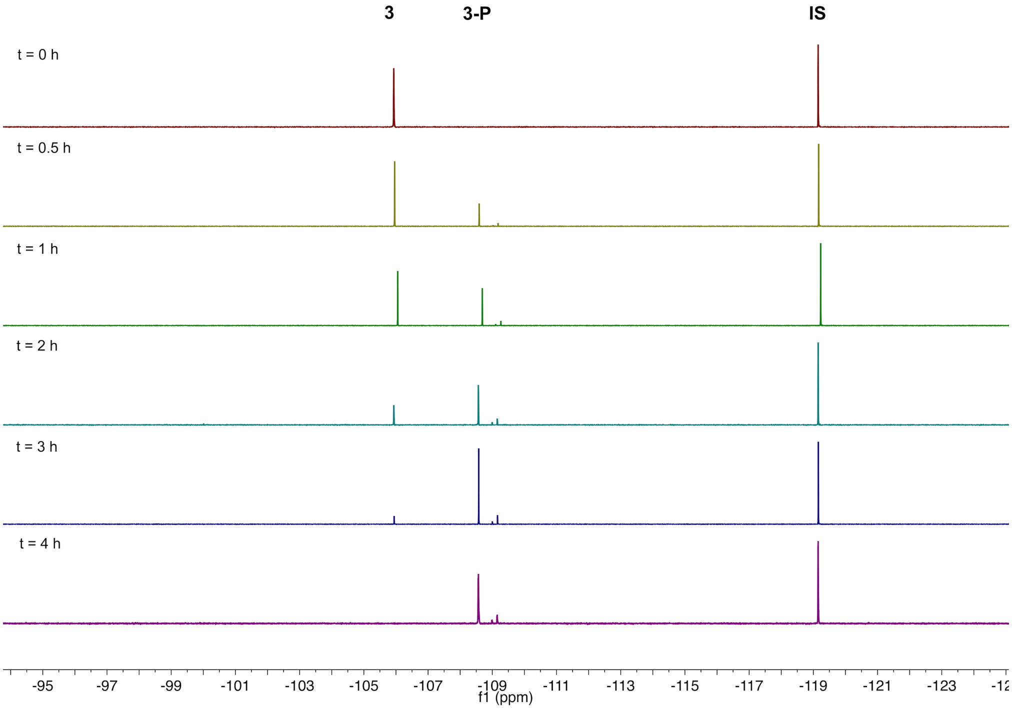

Figure S30. ^{19}F-NMR spectra monitoring debromination of substrate **3** over time using 447 nm cw-laser irradiation. Reaction conditions: 30 mM **3**, 1 mol% *fac*-[Ir(ppy)$_3$], 10 mol% ^{tBu}Py and 5 eq. DMA in DMF. IS = internal standard (4-fluorotoluene). Unassigned signals at -109.11 ppm and -109.28 ppm are unidentified side products most likely based on side reactions with DMA related degradation intermediates.

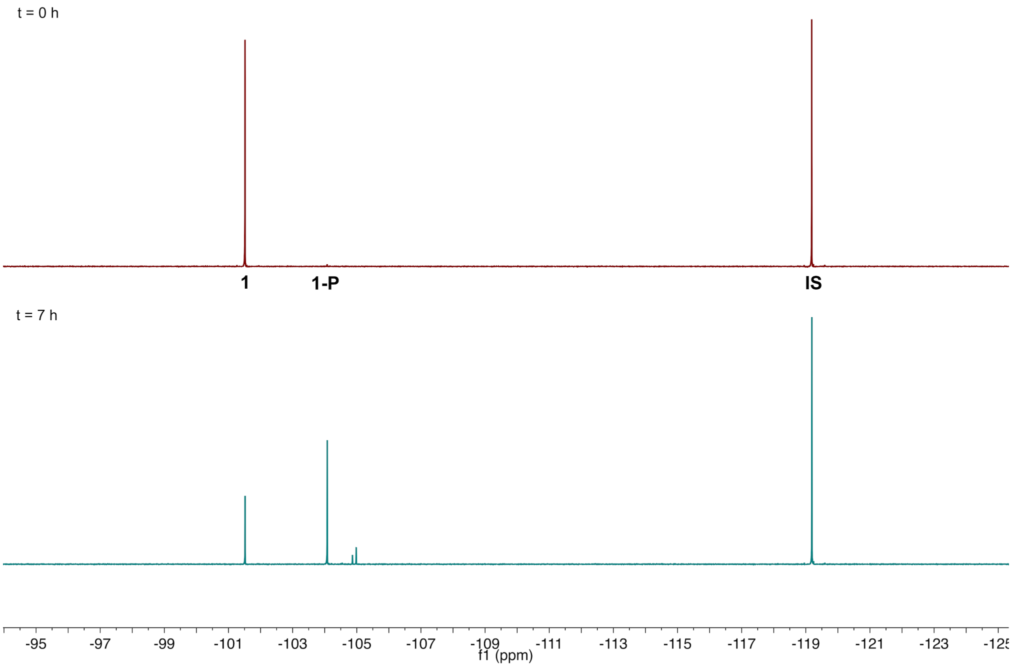

Figure S31. ^{19}F-NMR spectra monitoring dechlorination of substrate **1** over time using 440 nm LED irradiation. Reaction conditions: 30 mM **1**, 1 mol% *fac*-[Ir(ppy)$_3$], 10 mol% ^{tBu}Py and 5 eq. DMA in DMF. IS = internal standard (4-fluorotoluene). Unassigned signals at -104.85 ppm and -104.93 ppm are unidentified side products most likely based on side reactions with DMA related degradation intermediates.

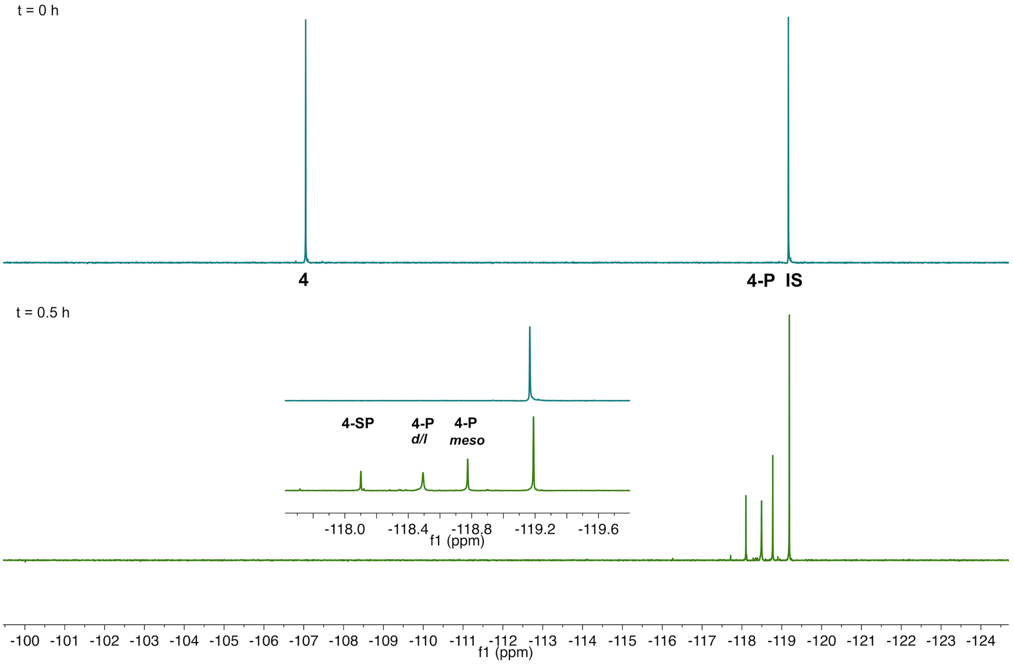

Figure S32. ^{19}F-NMR spectra monitoring dechlorination of substrate **4** over time using 440 nm LED irradiation. Reaction conditions: 30 mM **4**, 0.25 mol% *fac*-[Ir(ppy)$_3$], 10 mol% ^{tBu}Py and 5 eq. DMA in DMF. IS = internal standard (4-fluorotoluene); **4-SP** = 2-(4-fluorophenyl)-1-(methyl(phenyl)amino)propan-2-ol.

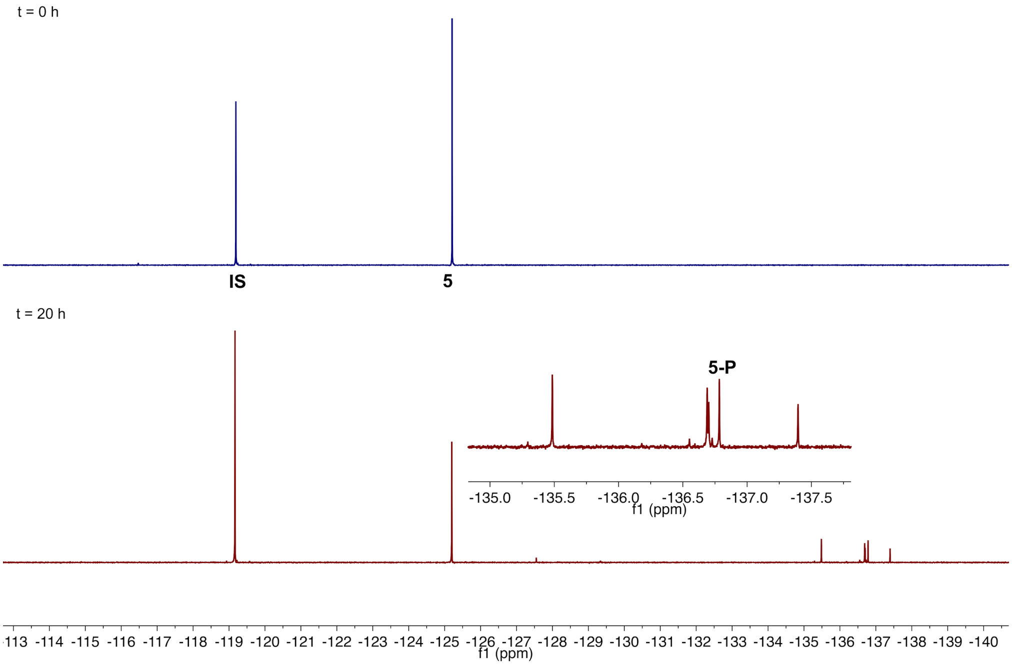

Figure S33. ^{19}F-NMR spectra monitoring dechlorination of substrate **5** over time using 440 nm LED irradiation. Reaction conditions: 30 mM **5**, 1 mol% *fac*-[Ir(ppy)$_3$], 10 mol% ^{tBu}Py and DMA (5 eq.) in DMF. IS = internal standard (4-fluorotoluene). Unassigned signals are unidentified side products.

6. References

1 H. E. Gottlieb, V. Kotlyar and A. Nudelman, *J. Org. Chem.*, 1997, **62**, 7512–7515.

2 C. Kerzig and O. S. Wenger, *Chem. Sci.*, 2018, **9**, 6670–6678.

3 F. Glaser, C. B. Larsen, C. Kerzig and O. S. Wenger, *Photochem. Photobiol. Sci.*, 2020, **19**, 1035–1041.

4 M. S. Mehata, Y. Yang, Z. J. Qu, J. S. Chen, F. J. Zhao and K. L. Han, *RSC Adv.*, 2015, **5**, 34094–34099.

5 P. Duan, N. Yanai and N. Kimizuka, *Chem. Commun.*, 2014, **50**, 13111–13113.

6 J. H. Kim, S. Y. Kim, D. W. Cho, H. J. Son and S. O. Kang, *Phys. Chem. Chem. Phys.*, 2019, **21**, 6908–6916.

7 B. Pfund, D. M. Steffen, M. R. Schreier, M.-S. Bertrams, C. Ye, K. Börjesson, O. S. Wenger and C. Kerzig, *J. Am. Chem. Soc.*, 2020, **142**, 10468–10476.

8 W. Zhao and F. N. Castellano, *J. Phys. Chem. A*, 2006, **110**, 11440–11445.

9 T. G. Pavlopoulos, *J. Chem. Phys.*, 1970, **52**, 3307–3308.

10 S. M. Bachilo and R. B. Weisman, *J. Phys. Chem. A*, 2000, **104**, 7713–7714.

11 I. Carmichael, W. P. Helman and G. L. Hug, *J. Phys. Chem. Ref. Data*, 1987, **16**, 239–260.

12 T. N. Singh-Rachford and F. N. Castellano, *Coord. Chem. Rev.*, 2010, **254**, 2560–2573.

13 M. S. Coles, G. Quach, J. E. Beves and E. G. Moore, *Angew. Chem.*, 2020, **132**, 9609–9613.

14 B. M. Wilke and F. N. Castellano, *J. Chem. Educ.*, 2013, **90**, 786–789.

15 A. Haefele, J. Blumhoff, R. S. Khnayzer and F. N. Castellano, *J. Phys. Chem. Lett.*, 2012, **3**, 299–303.

16 Y. Zhou, F. N. Castellano, T. W. Schmidt and K. Hanson, *ACS Energy Lett.*, 2020, **5**, 2322–2326.

17 A. M. Funston, S. V. Lymar, B. Saunders-Price, G. Czapski and J. R. Miller, *J. Phys. Chem. B*, 2007, **111**, 6895–6902.

18 R. G. Brown, A. Harriman and L. Harris, *J. Chem. Soc. Faraday Trans. 2 Mol. Chem. Phys.*, 1978, **74**, 1193–1199.

19 C. D. Borsarelli, J. J. Cosa and C. M. Previtali, *Photochem. Photobiol.*, 1998, **68**, 438–446.

20 F. Cao, J. Kim and A. J. Bard, *J. Am. Chem. Soc.*, 2014, **136**, 18163–18169.

21 T. Shida, *Electronic absorption spectra of radical ions*, Elsevier, Amsterdam; New York, 1988.

22 H. Masuhara and N. Mataga, *Acc. Chem. Res.*, 1981, **14**, 312–318.

23 H. Hirano and T. Azumi, *Chem. Phys. Lett.*, 1982, **86**, 100–104.

24 J. F. Delouis, J. A. Delaire and N. Ivanoff, *Chem. Phys. Lett.*, 1979, **61**, 343–346.

25 H. Schomburg, H. Staerk and A. Weller, *Chem. Phys. Lett.*, 1973, **22**, 1–4.

26 T. N. Das and K. I. Priyadarsini, *J. Chem. Soc. Perkin Trans. 2*, 1993, 733–739.

27 H. Shi, C. Du, X. Zhang, F. Xie, X. Wang, S. Cui, X. Peng, M. Cheng, B. Lin and Y. Liu, *J. Org. Chem.*, 2018, **83**, 1312–1319.

28 M. Paradas, A. G. Campaña, R. E. Estévez, L. Á. De Cienfuegos, T. Jiménez, R. Robles, J. M. Cuerva and J. E. Oltra, *J. Org. Chem.*, 2009, **74**, 3616–3619.

29 A. Chatterjee and B. König, *Angew. Chem., Int. Ed.*, 2019, **58**, 14289–14294.

30 A. K. Pal, C. Li, G. S. Hanan and E. Zysman-Colman, *Angew. Chem., Int. Ed.*, 2018, **57**, 8027–8031.